Science Advances
AAAS

advances.sciencemag.org/cgi/content/full/7/1/eabd3568/DC1

Supplementary Materials for

Liquid-liquid phase separation of light-inducible transcription factors increases transcription activation in mammalian cells and mice

Nils Schneider, Franz-Georg Wieland, Deqiang Kong, Alexandra A. M. Fischer, Maximilian Hörner, Jens Timmer, Haifeng Ye, Wilfried Weber*

*Corresponding author. Email: wilfried.weber@biologie.uni-freiburg.de

Published 1 January 2021, *Sci. Adv.* **7**, eabd3568 (2021)
DOI: 10.1126/sciadv.abd3568

This PDF file includes:

Referenced Supplementary Figures

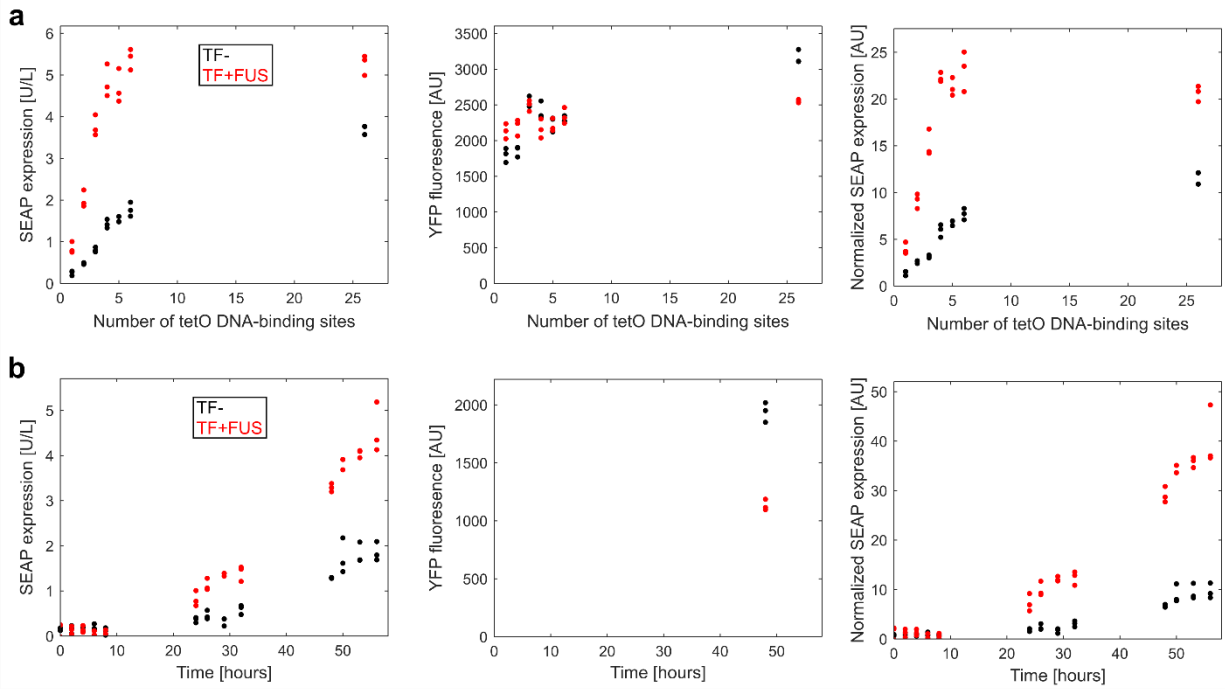

Figure S1. Raw data of SEAP production and transcription factor expression used to calculate normalized SEAP production in Figure 1 a. For varying amounts of tetO, SEAP production was measured via enzymatic activity (left) and transcription factor expression was measured via eYFP fluorescence and flow cytometry (middle). SEAP production was then normalized to transcription factor expression (right). b) Expression of SEAP (left), eYFP (middle) and normalized SEAP values (right) for temporal dynamics. eYFP expression was measured after 48 h, this measurement was used to normalize the SEAP measurements. AU, arbitrary units.

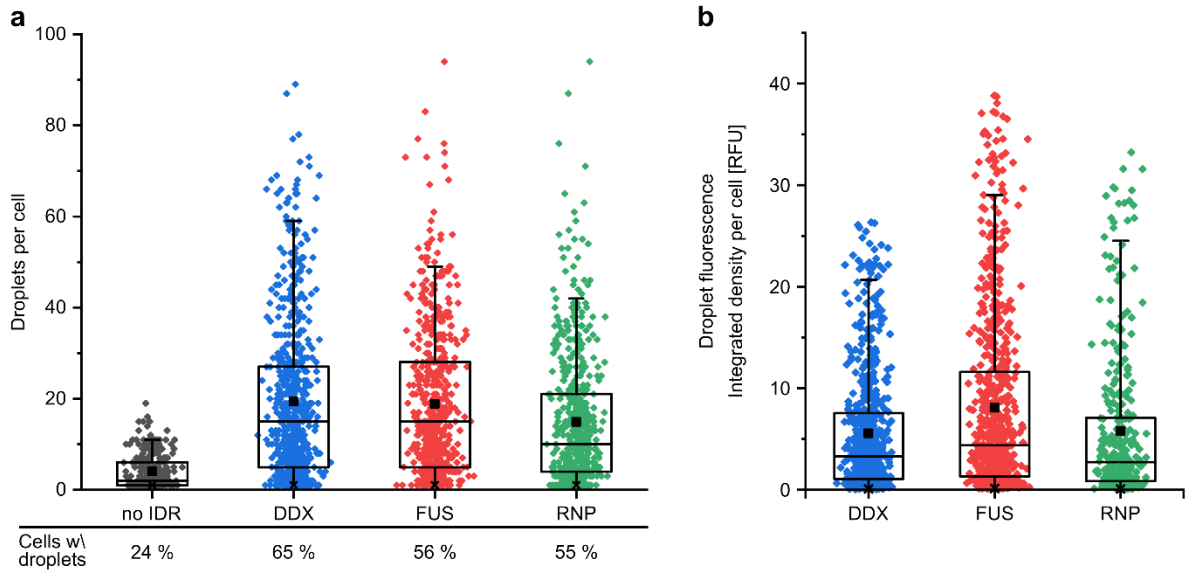

Figure S2. Distribution of OptoTF constructs in cells. Expression vectors for OptoTF- and three Opto+IDR were transfected into HEK-293 cells and cultivated under blue light (465 nm, 5 µmol m^{-2} s^{-1}) for 24 h prior to analysis by fluorescence microscopy. a) Percentage of cells with visible droplets (bottom line) as well as the number of visible droplets per cell. 1000 cells were analyzed. b) Integrated fluorescence intensity of droplets in cells. Median values: horizontal line; mean values: black squares; boxes: 50% of the population; whiskers: 90% of the population. RFU, relative fluorescent units.

a

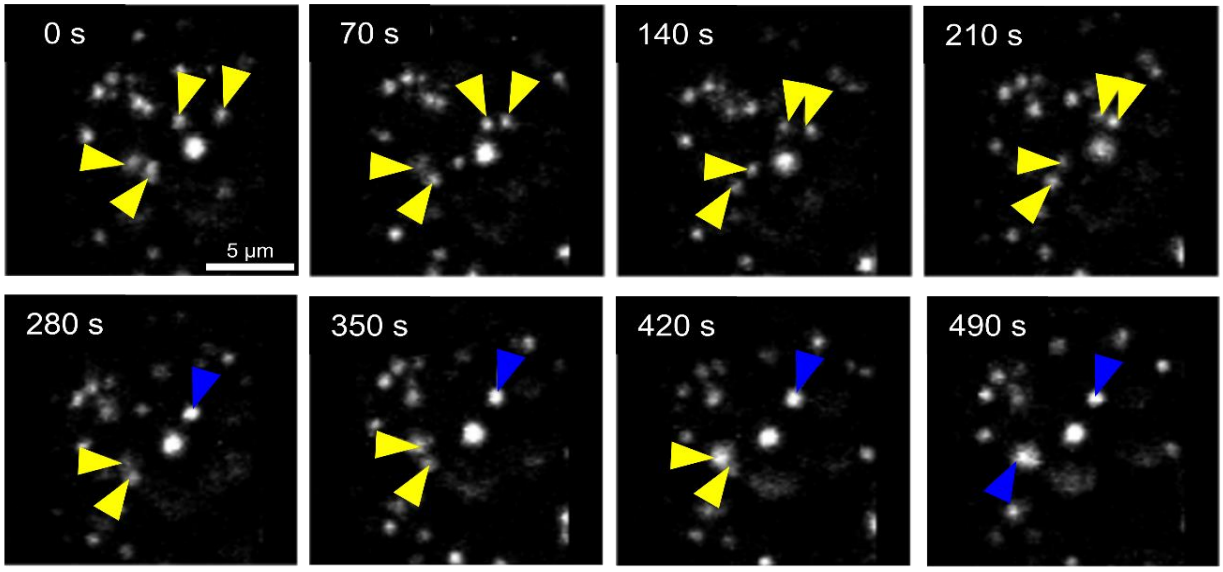
0 s
70 s
140 s
210 s
5 µm
280 s
350 s
420 s
490 s

b

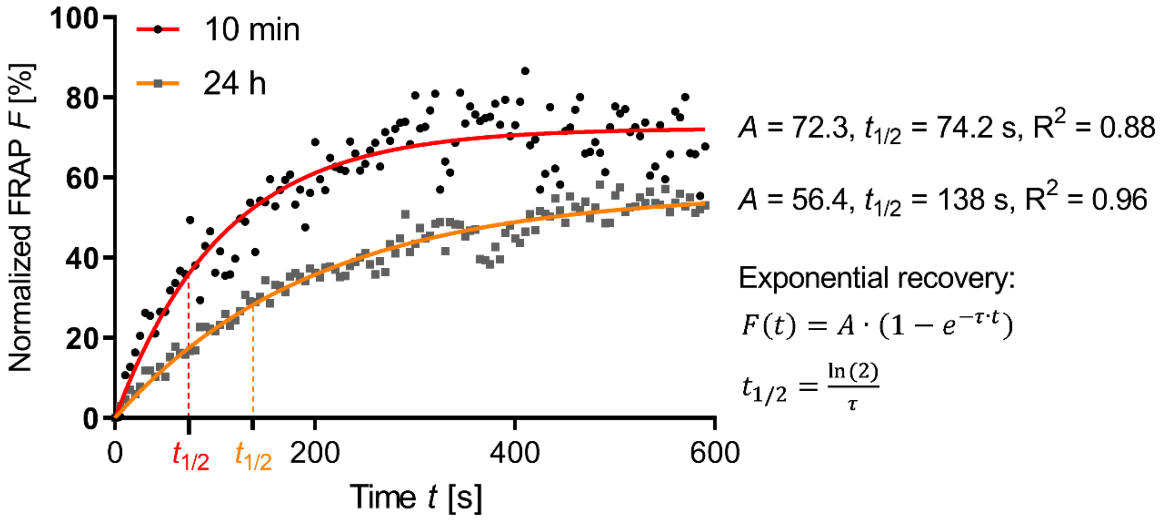
10 min
24 h
Normalized FRAP F [%]
100
80
60
40
20
0
0
$t_{1/2}$
$t_{1/2}$
200
400
600
Time t [s]
A = 72.3, $t_{1/2}$ = 74.2 s, R^2 = 0.88
A = 56.4, $t_{1/2}$ = 138 s, R^2 = 0.96
Exponential recovery:
$F(t) = A \cdot (1 - e^{-\tau \cdot t})$
$t_{1/2} = \frac{\ln(2)}{\tau}$

c

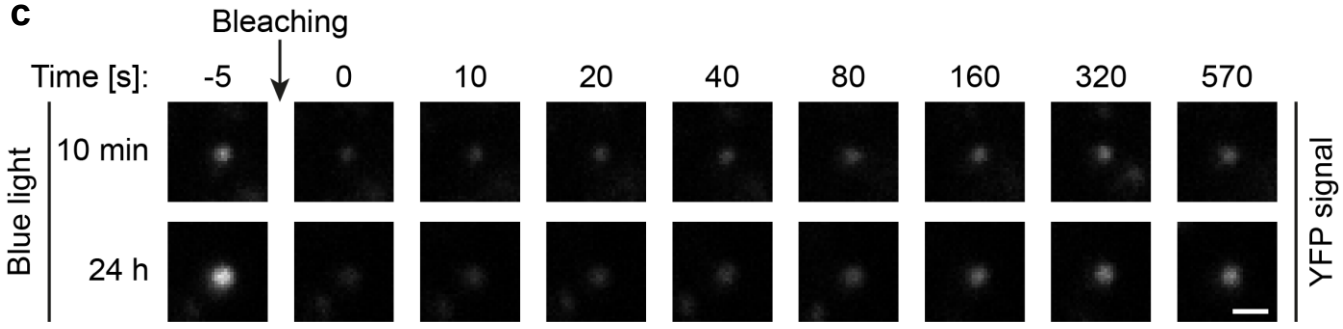
Bleaching
Time [s]:
-5
0
10
20
40
80
160
320
570
Blue light
10 min
24 h
YFP signal

d

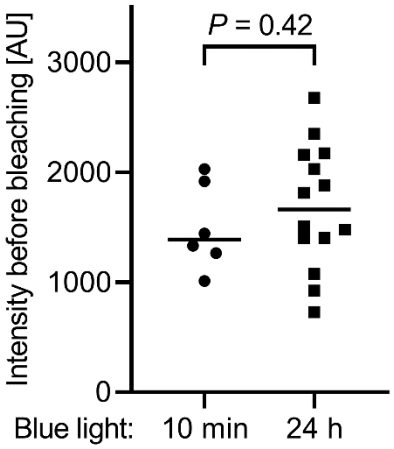

Figure S3. Liquid properties of OptoTF+FUS droplets. a) Fusion event of two droplets. OptoTF+FUS was transfected into HEK-293 cells. 24 h after transfection, HEK-293 cells were illuminated for 3 min with blue light (465 nm, 5 µmol m^{-2} s^{-1}) followed by live cell imaging of eYFP flurescence at 70 s intervals via confocal microscopy. Yellow arrowheads indicate droplets in close proximity that combine into single, larger droplets, indicated by blue arrowheads. b) Representative FRAP recovery curves of experiment depicted in Figure 2 c. FRAP was performed after 10 min (red) or 24 h (orange) blue light illumination. c) Representative images of droplet bleaching. Scale bar, 1 µm. d) Intensity of the droplets before bleaching. Both groups were compared by a two-tailed Welch's t test. AU, arbitrary units.

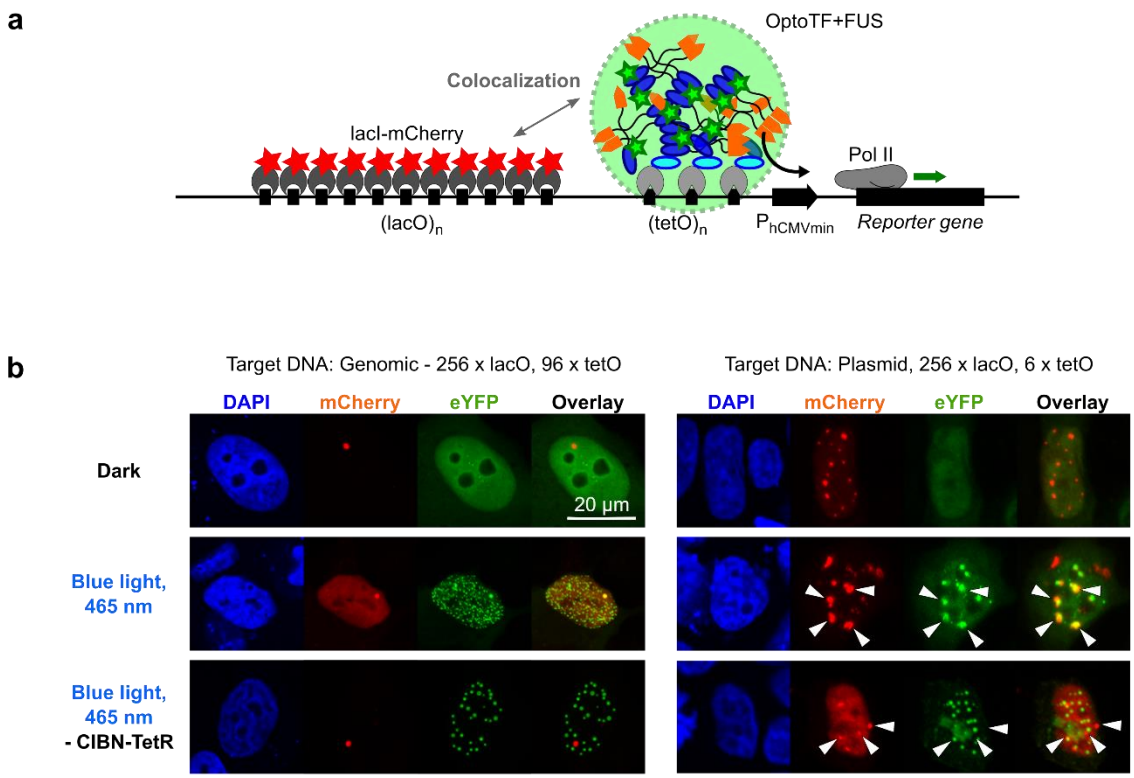

Figure S4. Localization of DropletTFs on reporter DNA. a) Mode of function of the localization assay: the DNA upstream the promoter region is stained by binding of LacI-mCherry to lacO multimers. Yellow fluorescent OptoTF+FUS forms a coacervate at the multimeric tetO binding site. (Co-) localization of fluorescence is analyzed via confocal fluorescence microscopy. b) Left: Localization of mCherry-lacI and OptoTF+FUS on a genomic $lacO_{256}$ - $tetO_{96}$ array. U2OS cells were transfected with mCherry-lacI, OptoTF+FUS, and CIBn-TetR. 24 h after transfection, cells were illuminated for 24 h with blue light (465 nm, 5 µmol m^{-2} s^{-1}) prior to analysis by fluorescence microscopy. Right: Localization of mCherry-lacI and OptoTF+FUS on transiently transfected reporter plasmids harboring $lacO_{256}$ - $tetO_6$. HEK-293 cells were transfected with mCherry-lacI, OptoTF+FUS, CIBn-TetR, and reporter $lacO_{256}$_$tetO_6$_SEAP. 24 h after transfection, cells were illuminated for 24 h with blue light (465 nm, 5 µmol m^{-2} s^{-1}) prior to analysis by confocal fluorescence microscopy.

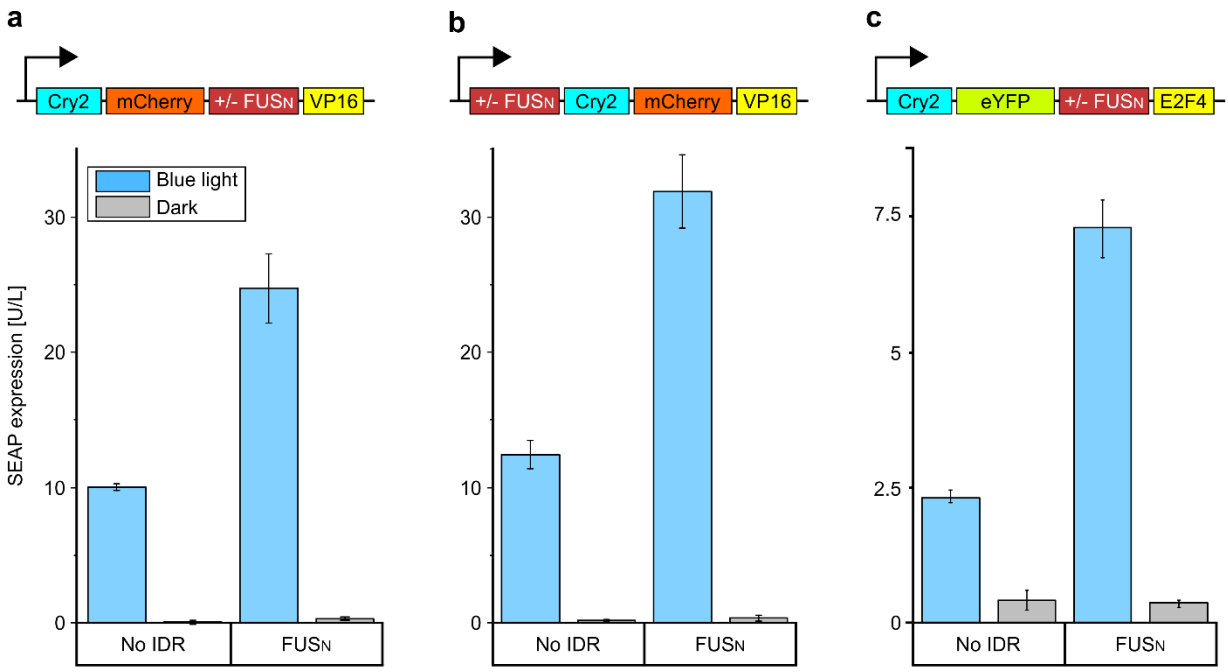

Figure S5. Effects of FUS insertion into OptoTF constructs fluorescently labeled with mCherry and exchange of the transactivation-domain. HEK-293 cells were co-transfected with the indicated constructs, a TetR-CIBn construct, and a $tetO_7$-based SEAP reporter. Cells were cultivated in the dark or under blue light (465 nm, 5 µmol m^{-2} s^{-1}) for 48 h prior to quantifying SEAP production. a) FUSn between Cry2-mCherry and VP16. b) FUSn at the N-terminus of Cry2-mCherry-VP16. c) Exchange of the VP16 TAD with the E2F4 TAD.

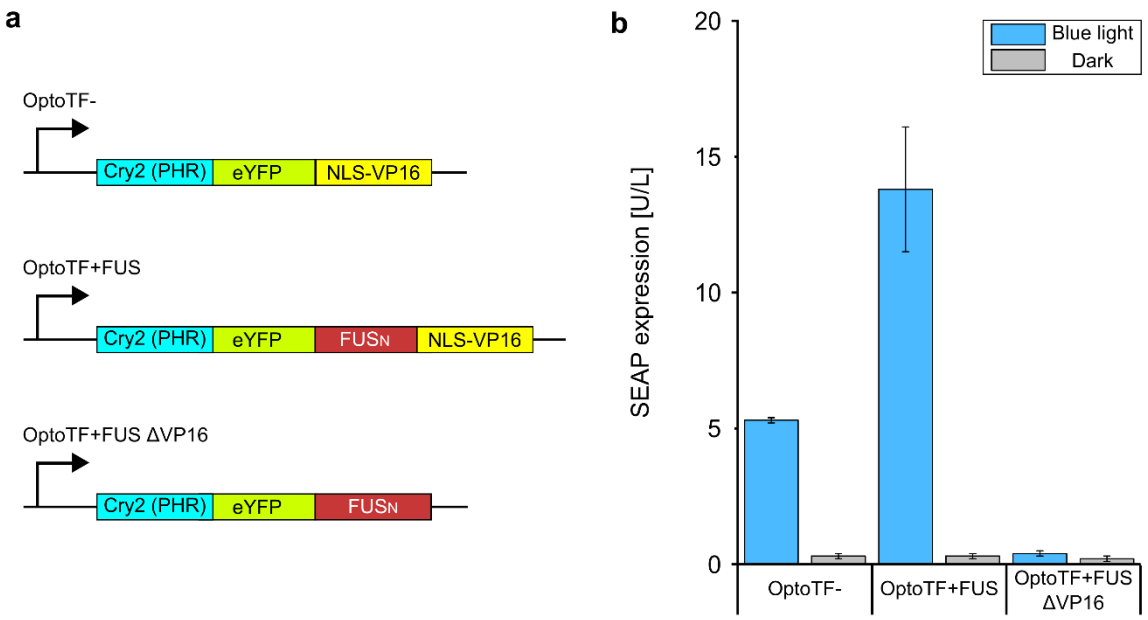

Figure S6. Investigation of the effect of FUSn on gene expression. a) OptoTF constructs tested. b) HEK-293 cells were co-transfected with the indicated constructs, a TetR-CIBn construct, and a $tetO_7$-based SEAP reporter. Cells were cultivated in the dark or under blue light (465 nm, 5 µmol m^{-2} s^{-1}) for 24 h prior to quantifying SEAP production.

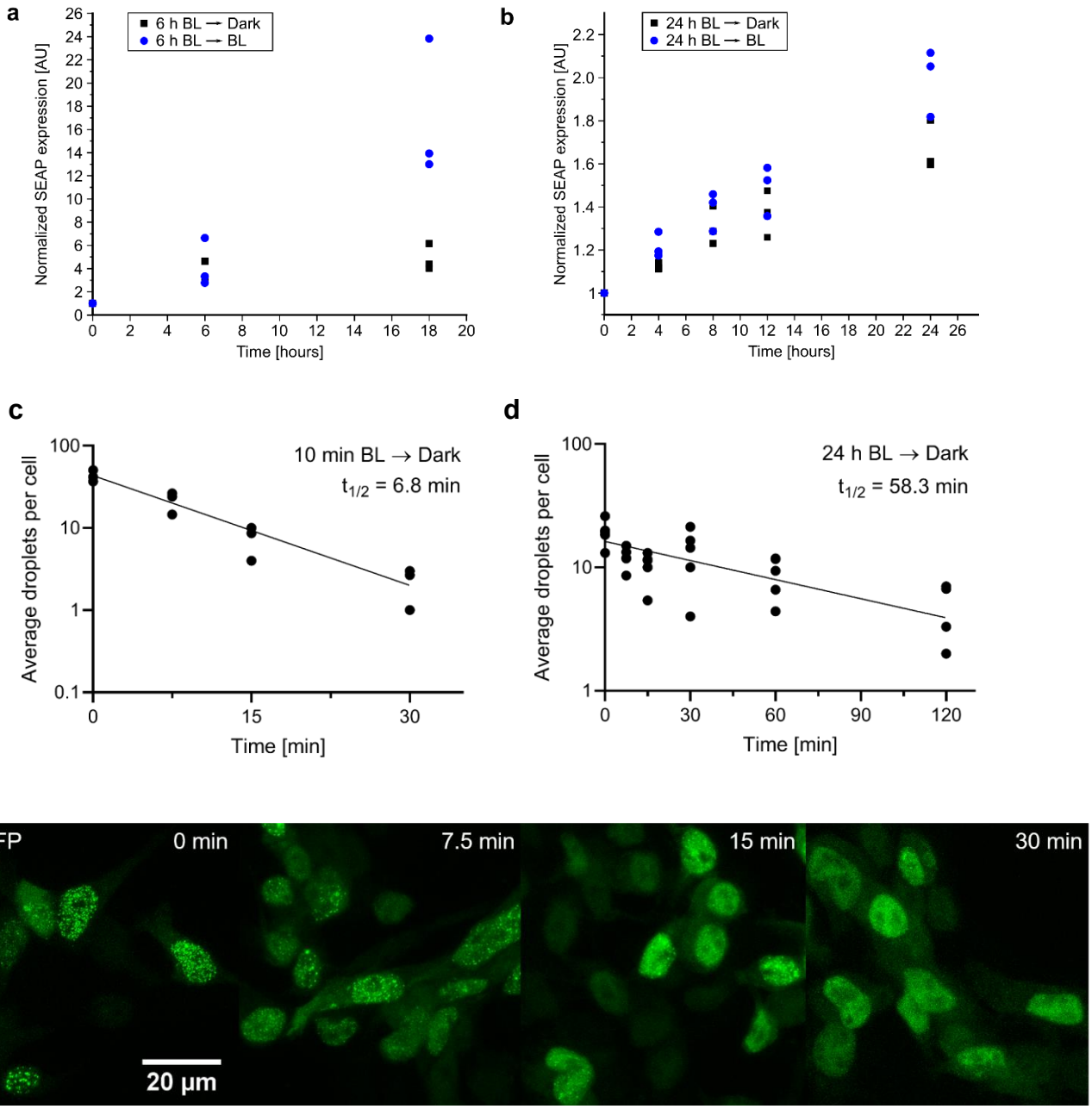
a
6 h BL → Dark
6 h BL → BL
Normalized SEAP expression [AU]
Time [hours]
b
24 h BL → Dark
24 h BL → BL
Normalized SEAP expression [AU]
Time [hours]
c
10 min BL → Dark
t1/2 = 6.8 min
Average droplets per cell
Time [min]
d
24 h BL → Dark
t1/2 = 58.3 min
Average droplets per cell
Time [min]
e
eYFP
0 min
7.5 min
15 min
30 min
20 µm

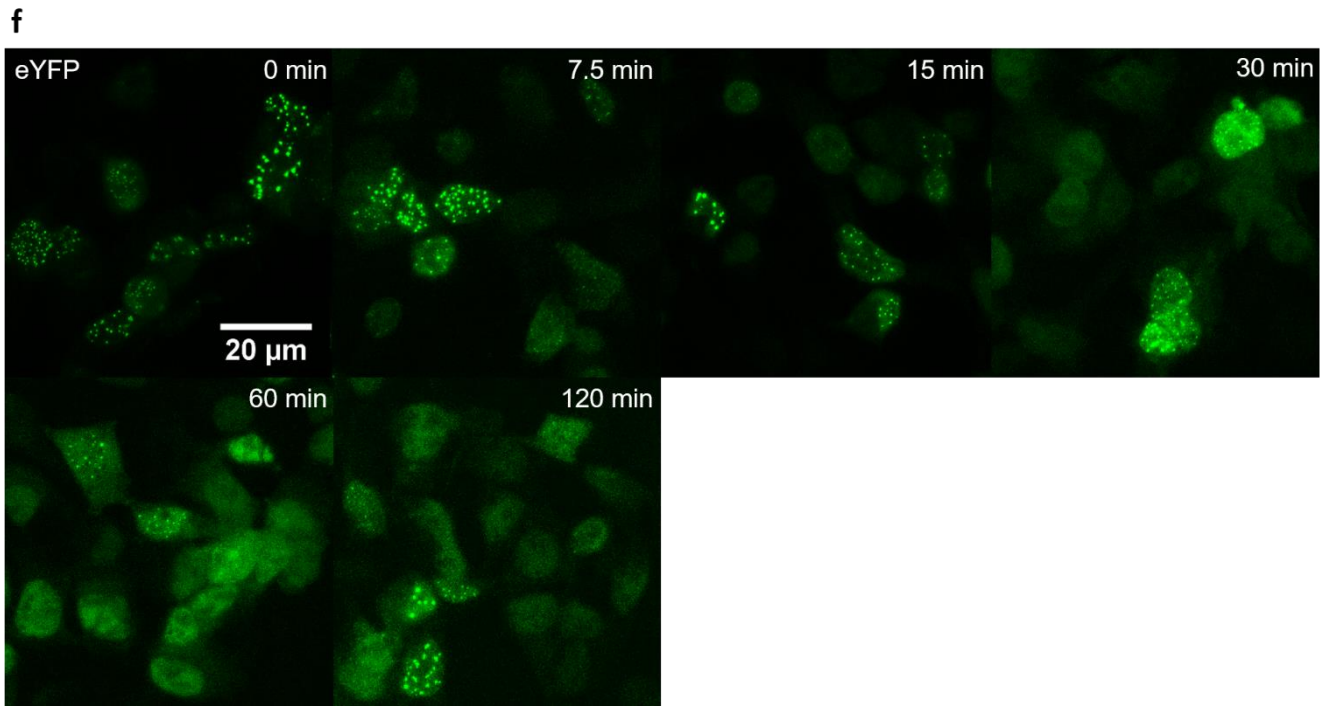

Figure S7. Reversibility of OptoTF+FUS condensates. a, b) Reversibility of gene expression. OptoTF+FUS and CIBn-TetR were transfected into HEK-293 cells together with a $tetO_7$-based SEAP reporter. 24 h after transfection, cells were illuminated with blue light (465 nm, 5 µmol m^{-2} s^{-1}) for a) 6 h or b) 24 h before they were transferred into dark (t_0 = 0 h). SEAP values were normalized to t_0. AU, arbitrary units. c – f) Disassembly of OptoTF+FUS droplets. OptoTF+FUS, CIBn-TetR and a $tetO_7$-based SEAP reporter were transfected into HEK-293 cells. 24 h later, cells were illuminated for c, e) 10 min or d, f) 24 h with blue light (465 nm, 5 µmol m^{-2} s^{-1}) before they were transferred into dark. Cells were fixed for microscopy at the indicated time points. Average number of droplets per cell with droplets was determined and $t_{1/2}$ was calculated. Data was fitted to a one phase exponential decay using non-linear regression. 95% confidence intervals are for c) 5.0 to 9.1 min and for d) 34.7 to 108.4 min.

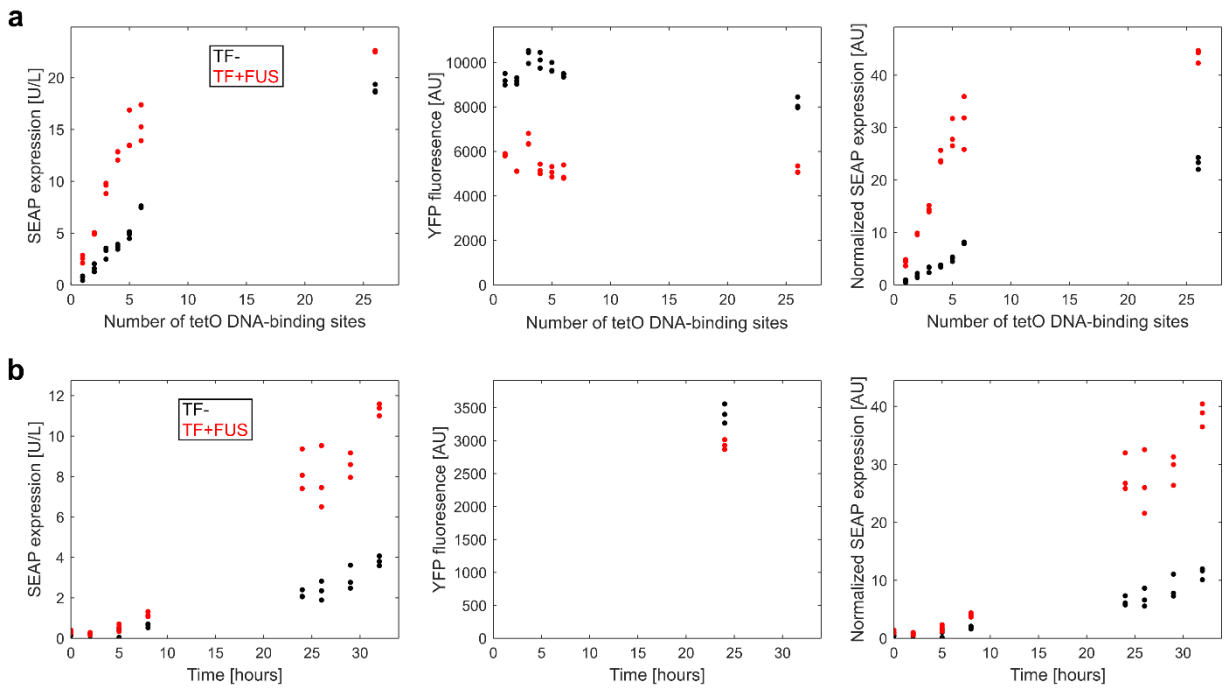

Figure S8. Raw data of SEAP production and transcription factor expression used to calculate normalized SEAP production in Figure 3 a) For varying numbers of tetO, SEAP production was measured via enzymatic activity (left) and transcription factor expression was measured via eYFP fluorescence and flow cytometry (middle). SEAP production was then normalized to transcription factor expression (right). b) Expression of SEAP (left), eYFP (middle) and normalized SEAP values (right) for temporal dynamics. eYFP expression was measured after 24 h and this measurement used to normalize all SEAP measurements. AU, arbitrary units.

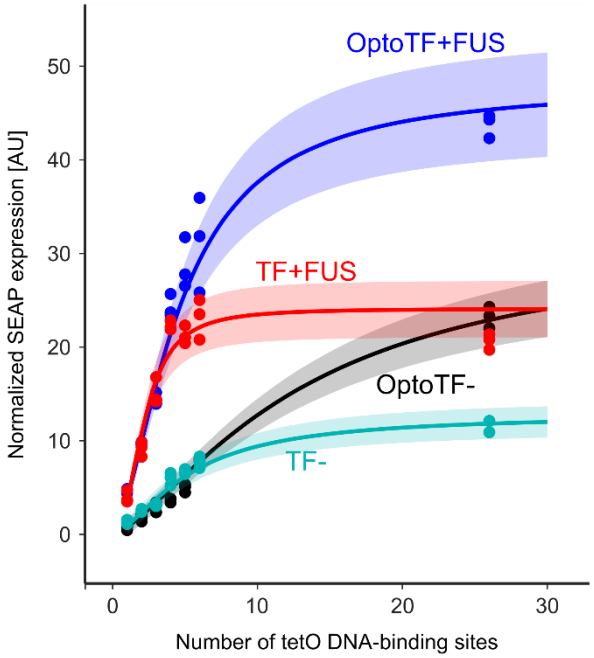

Figure S9. Combined data of Figure 1 c and Figure 3 b. $tetO_n$-based SEAP reporters (n = 1-6, 26) were co-transfected into HEK-293 cells with TF-, TF+FUS, OptoTF-, and OptoTF+FUS expression constructs. The stoichiometry of the expression vectors was adjusted so that TF- and TF+FUS as well as OptoTF- and OptoTF+FUS were produced at equal amounts per cell. SEAP production was quantified after 48 h. In parallel, TF expression levels were determined by flow cytometry of eYFP. To account for variations in TF expression, SEAP production values were normalized to YFP fluorescence values. The model fit is derived from the extended model including both datasets. The model fit to the data is represented by the curves while the shaded error bands are estimated with an error model with a constant and relative Gaussian error. AU, arbitrary units.

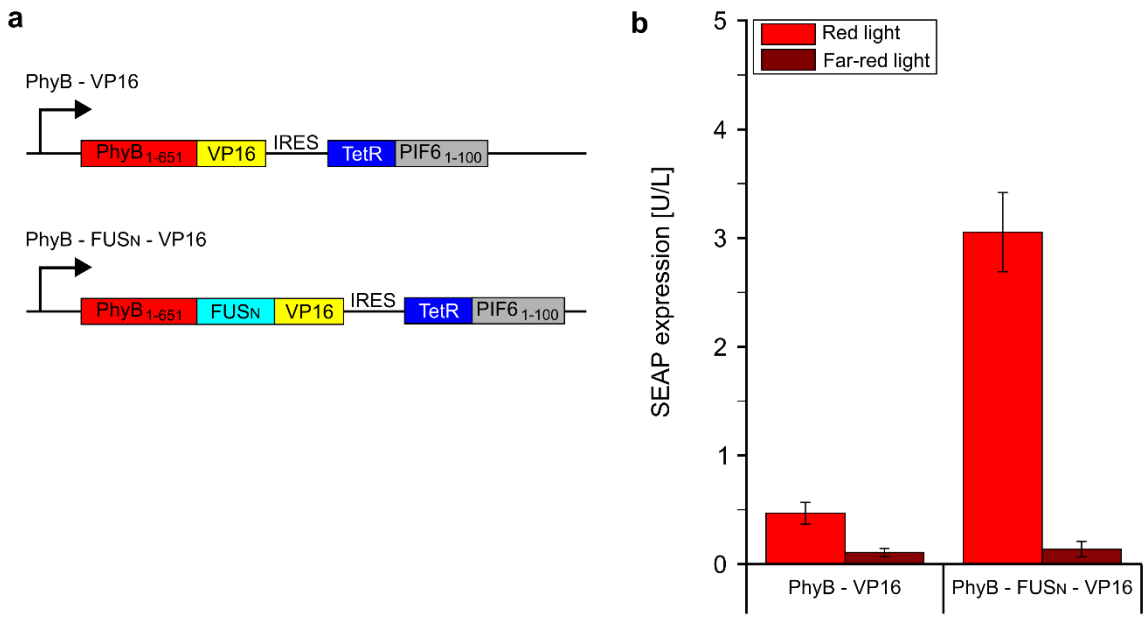

Figure S10. Red light-responsive OptoTF system. a) Design of the constructs. *Arabidopsis* phytochrome B (PhyB, amino acids 1-651) is fused to VP16 or to FUSn-VP16. This gene is expressed from a bicistronic construct together with TetR fused to the phytochrome interacting factor PIF6 (amino acids 1-100). b) Performance of the red light-responsive OptoTF system. The constructs indicated in a) were co-transfected with a $tetO_7$-based SEAP reporter into HEK-293 cells. Cells were cultivated for 24 h under red (660 nm, 10 µmol m^{-2} s^{-1}) or far-red (740 nm, 100 µmol m^{-2} s^{-1}) light prior to quantifying SEAP production. Experiments were conducted as described before.[1]

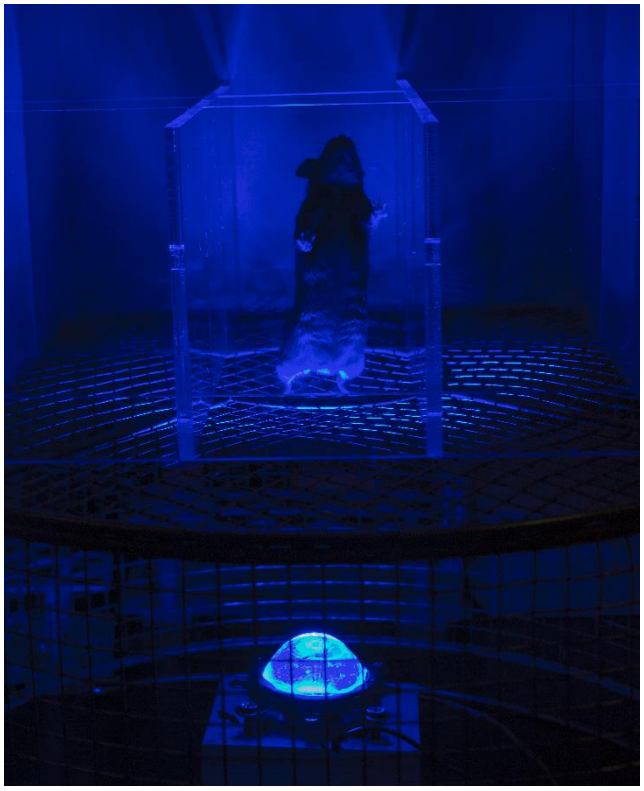

Figure S11. Mouse illumination device. Mice are illuminated with a LED (50 W, 45 miL, 460-470 nm, with the light angle 60°) which was obtained from Shenzhen Kiwi Lighting Co. Ltd. This integrated LED contains 50 small LED (1W) beads. The light intensity was measured at a wavelength of 465 nm using an optical power meter (Q8230; Advantest) according to the manufacturer's operating specifications. (Photo Credit: Deqiang Kong, East China Normal University)

Illumination Intensity: 5 mW cm^{-2}

OptoTF-

OptoTF + FUS

Illumination Intensity: 10 mW cm^{-2}

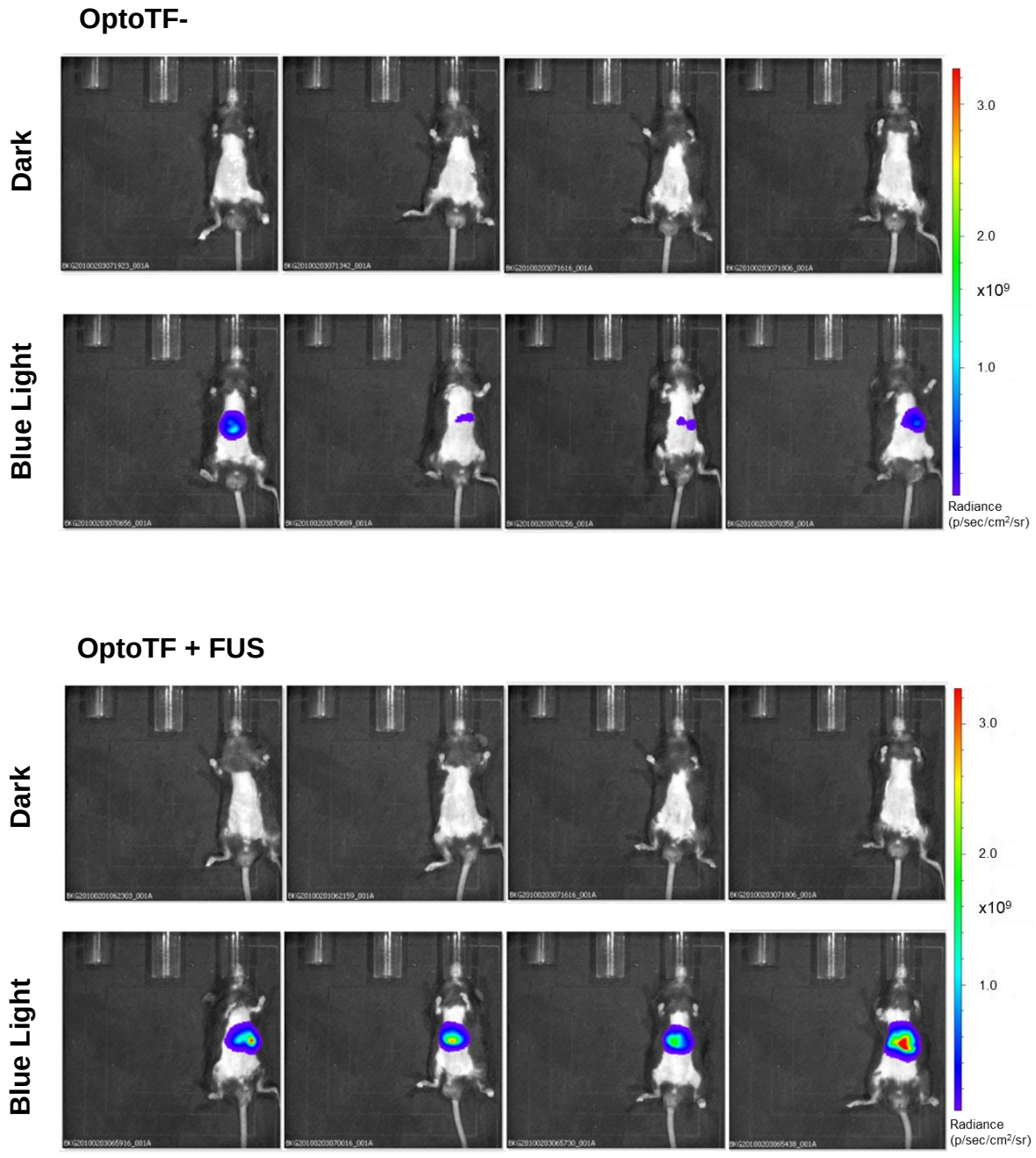

Figure S12. Raw data of luciferase expression shown in Figure 4 c. The reporter construct tetO$_7$-Luciferase was co-transfected with CIBn-TetR and either OptoTF- or OptoTF+FUS constructs via the tail vein. Eight hours after plasmid injection, the mice were kept in the dark or exposed to blue light pulses for 11 h (460 nm LED; 2 min on, 2 min off, alternating) at an intensity of 5 mW cm^{-2} or 10 mW cm^{-2} (for each light intensity and condition 4 mice were kept in the dark and 4 mice were kept under light). For *in vivo* bioluminescence imaging, each mouse was intraperitoneally injected with luciferin substrate under ether anaesthesia. Five minutes after luciferin injection,

bioluminescence radiance (p sec^{-1} cm^{-2} sr^{-1}) was calculated for the region of interest. (Photo Credit: Deqiang Kong, East China Normal University)

Vector Information and Transfection Conditions

Table S1: Vectors used and developed in this study.

Plasmid	Backbone	Description
TF- (pNS089)	pEGFP-C3 (Clontech)	TetR-VP16-eYFP
TF+FUS (pNS091)	pEGFP-C3	TetR-VP16-FUSn-eYFP
ClBn-TetR (pNS1000)	pEGFP-C3	ClBn-TetR
OptoTF- (pNS1001)	pEGFP-C3	Cry2-eYFP-VP16
OptoTF+DDX (pNS025)	pEGFP-C3	Cry2-eYFP-DDX-VP16
OptoTF+FUS (pNS026)	pEGFP-C3	Cry2-eYFP-FUS-VP16
OptoTF+RNP (pNS027)	pEGFP-C3	Cry2-eYFP-RNP-VP16
OptoTF+FUS_Nterm (pNS038)	pEGFP-C3	FUS-Cry2-eYFP-VP16
OptoTF-_E2F4-TAD (pNS046)	pEGFP-C3	Cry2-eYFP-E2F4
OptoTF+FUS_E2F4-TAD (pNS075)	pEGFP-C3	Cry2-eYFP-FUS-E2F4
OptoTF+FUS_ΔVp16 (pNS043)	pEGFP-C3	Cry2-eYFP-FUS
OptoTF-_mC (pNS032)	pEGFP-C3	Cry2-mCherry-VP16
OptoTF+FUS_mC (pNS034)	pEGFP-C3	Cry2-mCherry-FUS-VP16
OptoTF+FUS_Nterm_mC (pNS041)	pEGFP-C3	FUS-Cry2-mCherry-VP16
tetO1_SEAP (pNS301)	pKM001	$tetO_1$-$P_{hCMVmin}$-SEAP
tetO2_SEAP (pNS302)	pKM001	$tetO_2$-$P_{hCMVmin}$-SEAP
tetO3_SEAP (pNS303)	pKM001	$tetO_3$-$P_{hCMVmin}$-SEAP
tetO4_SEAP (pNS304)	pKM001	$tetO_4$-$P_{hCMVmin}$-SEAP
tetO5_SEAP (pNS305)	pKM001	$tetO_5$-$P_{hCMVmin}$-SEAP
tetO6_SEAP (pNS306)	pKM001	$tetO_6$-$P_{hCMVmin}$-SEAP
tetO7_SEAP (pKM001) [4]	-	$tetO_7$-$P_{hCMVmin}$-SEAP
tetO26_SEAP (pKM004) [4]	pKM001	$tetO_{26}$-$P_{hCMVmin}$-SEAP
tetO13_mCherry (pKM078) [4]	-	$tetO_{13}$-$P_{hCMVmin}$-mCherry
lacO256_tetO6_SEAP (pNS053)	pKM001	$lacO_{256}$-$tetO_6$-$P_{hCMVmin}$-SEAP
pN2-mCherryLacI	-	mCherry-lacI
PhyB-VP16 (pKM022) [4]	-	PhyB-VP16_PIF-TetR
PhyB-FUS-VP16 (pNS072)	pKM022	PhyB-FUS-VP16_TetR-PIF
PhyB-FUS-eYFP-VP16-IRES-TetR-PIF6 (pNS098)	pKM022	PhyB-FUS-eYFP-VP16-IRES-TetR-PIF6
tetO7_Luciferase (pAF101)	pKM001	$tetO_7$-$P_{hCMVmin}$-Luciferase

Table S2: Plasmids encoding functional components and quantities transfected per 24-well for all biological data presented in this publication.

Figure	Condition	Plasmids and DNA amount
Fig 1 c	TF-	Reporter: pNS301-306, pKM004 (550 ng). Transcription factor: pNS089 (30 ng)

	TF+FUS	Reporter: pNS301-306, pKM004 (550 ng). Transcription factor: pNS091 (200 ng)
Fig 1 d	TF-	Reporter: pNS301-306, pKM004 (550 ng). Transcription factor: pNS089 (30 ng)
	TF+FUS	Reporter: pNS301-306, pKM004 (550 ng). Transcription factor: pNS091 (200 ng)
Fig 2 b	No IDR	Reporter: pKM078 (350 ng), DNA-binding domain: pNS1000 (200 ng), Transcription factor: pNS1001 (20 ng)
	DDX4N	Reporter: pKM078 (350 ng), DNA-binding domain: pNS1000 (200 ng), Transcription factor: pNS025 (20 ng)
	FUSN	Reporter: pKM078 (350 ng), DNA-binding domain: pNS1000 (200 ng), Transcription factor: pNS026 (20 ng)
	RNPAC	Reporter: pKM078 (350 ng), DNA-binding domain: pNS1000 (200 ng), Transcription factor: pNS027 (20 ng)
Fig 2 c	OptoTF+FUS	Reporter: pKM001 (500 ng), DNA-binding domain: pNS1000 (20 ng), Transcription factor: pNS026 (20 ng)
Fig 3 a	Cry2-eYFP-VP16	Reporter: pKM001 (350 ng), DNA-binding domain: pNS1000 (200 ng), Transcription factor: pNS1001 (20 ng)
	Cry2-eYFP-FUSn-VP16	Reporter: pKM078 (350 ng), DNA-binding domain: pNS1000 (200 ng), Transcription factor: pNS026 (20 ng)
	FUSn-Cry2-eYFP-VP16	Reporter: pKM078 (350 ng), DNA-binding domain: pNS1000 (200 ng), Transcription factor: pNS038 (20 ng)
Fig 3 b	OptoTF-	Reporter: pNS301-306, pKM004 (530 ng), DNA-binding domain: pNS1000 (20 ng), Transcription factor: pNS1001 (200 ng)
	OptoTF+FUS	Reporter: pNS301-306, pKM004 (530 ng), DNA-binding domain: pNS1000 (20 ng), Transcription factor: pNS026 (30 ng)
Fig 3 c	OptoTF-	Reporter: pNS304 (530 ng), DNA-binding domain: pNS1000 (20 ng), Transcription factor: pNS1001 (200 ng)
	OptoTF+FUS	Reporter: pNS304 (530 ng), DNA-binding domain: pNS1000 (20 ng), Transcription factor: pNS026 (30 ng)

Fig 4 b	OptoTF-	Reporter: pKM001 (500 ng), DNA-binding domain: pNS1000 (20 ng), Transcription factor: pNS1001 (20 ng)
	OptoTF+FUS	Reporter: pKM001 (500 ng), DNA-binding domain: pNS1000 (20 ng), Transcription factor: pNS026 (20 ng)
Fig S1 a,b	TF-	See Fig 1 c
	TF+FUS	See Fig 1 d
Fig S2 a,b	No IDR, DDX4N, FUSN, RNPC	See Fig 2 b
Fig S3 a	TF+FUS	Reporter: pKM078 (350 ng), DNA-binding domain: pNS1000 (200 ng), Transcription factor: pNS026 (20 ng)
Fig S3 b-d	OptoTF+FUS	Reporter: pKM001 (500 ng), DNA-binding domain: pNS1000 (20 ng), Transcription factor: pNS026 (20 ng)
Fig S4 b	Genomic target DNA	Marker: pN2-mCherryLacI (250 ng), DNA-binding domain: pNS1000 (0 or 250 ng), Transcription factor: pNS026 (250 ng)
	Plasmid target DNA	Reporter: pNS053 (450), Marker: pN2-mCherryLacI (100 ng), DNA-binding domain: pNS1000 (0 or 100 ng), Transcription factor: pNS026 (100 ng)
Fig S5 a	No IDR / FUSN	Reporter: pKM001 (530 ng), DNA-binding domain: pNS1000 (200 ng), Transcription factor: pNS032 (20 ng) / pNS034 (20 ng)

Fig S5 b	No IDR / FUSN	Reporter: pKM001 (530 ng), DNA-binding domain: pNS1000 (200 ng), Transcription factor: pNS032 (20 ng) / pNS41 (20 ng)
Fig S5 c	No IDR / FUSN	Reporter: pKM001 (530 ng), DNA-binding domain: pNS1000 (200 ng), Transcription factor: pNS046 (20 ng) / pNS75 (20 ng)
Fig S6 b	OptoTF-	Reporter: pKM001 (350 ng), DNA-binding domain: pNS1000 (200 ng), Transcription factor: pNS1001 (200 ng)
	OptoTF+FUS	Reporter: pKM001 (350 ng), DNA-binding domain: pNS1000 (200 ng), Transcription factor: pNS026 (200 ng)
	OptoTF+FUSΔVP16	Reporter: pKM001 (350 ng), DNA-binding domain: pNS1000 (200 ng), Transcription factor: pNS043 (200 ng)
Fig S7	OptoTF+FUS	Reporter: pKM001 (500 ng), DNA-binding domain: pNS1000 (20 ng), Transcription factor: pNS026 (20 ng)
Fig S8 a,b	OptoTF-	See Fig 3 b
	OptoTF+FUS	See Fig 3 c
Fig S9	TF-, TF+FUS, OptoTF-, OptoTF +FUS	See Fig 1 c and Fig 3 b
Fig S10 b	PhyB-VP16	Reporter: pKM001 (730 ng), DNA-binding domain + Transcription factor: pKM022 (20 ng)
	PhyB-FUSN-VP16	Reporter: pKM001 (730 ng), DNA-binding domain + Transcription factor: pNS072 (20 ng)

Supplementary Information - Modelling.

Section 1) Development of the mathematical model for DropletTF

a. Derivation of the set of ordinary differential equations (ODEs).

In the following chapter, we derive the mathematical model describing the TF- and TF+FUS transcription factors and the transcription of the reporter SEAP mRNA and translation of SEAP from its mRNA based on ODEs.

The transcription factors TF- and TF+FUS binding to the tetO sites lead to a transcription of $SEAP_{mRNA}$. This is modelled by a Michalis-Menten reaction with the reaction rate k^*_{transk} and the Michaelis-Menten constant K^*_m, dependent on the concentration of tetO in the cells. The parameter k^*_{transk} defines the limit behaviour of the reaction. For high concentrations of tetO the concentration of $SEAP_{mRNA}$ asymptotically approaches k^*_{transk}. K^*_m on the other hand, defines the concentration of tetO, for which $SEAP_{mRNA}$ reaches half this limit concentration, thus governing the transient behaviour of the dose-response curve.
These two parameters can differ for the TF- and the TF+FUS transcription factors. Thus, two distinct effects have to be modelled, depending on the existence of either TF- or TF+FUS. This is denoted in the asterisk of the parameters. This asterisk encapsulates the fact that separate parameters k^{TF-}_{transk} and k^{TF+FUS}_{transk} as well as K^{TF-}_m and K^{TF+FUS}_m exist. The cooperativity of the reaction is modelled with the Hill parameter h^*, which again is dependent on the transcription factor.
SEAP mRNA is degraded with the rate $k_{deg,SEAP_{mRNA}}$. This rate is independent of the transcription factor and thus only one parameter for it exists. The basal transcription of $SEAP_{mRNA}$ can be neglected because of the short timescale of the experiments and the high transcription rates due to the transcription factors TF- and TF+FUS.
Thus, the ODE describing the dynamic concentration behavior of $SEAP_{mRNA}$ is

$$\frac{d[SEAP_{mRNA}](t)}{dt} = \frac{k^*_{transk}\,[tetO]^{h^*}}{(K^*_m)^{h^*} + [tetO]^{h^*}} - k_{deg,SEAP}\,[SEAP_{mRNA}], \tag{1.1}$$

where the asterisk are replaced by TF- or TF+FUS, depending on the experimental setup.

$SEAP_{mRNA}$ leads to a translation of the target protein SEAP with the rate $k_{transl,SEAP}$. The degradation of SEAP can be neglected, because it happens on a much slower timescale than the experiments. Thus, the ODE describing the dynamic behavior of the SEAP concentration becomes

$$\frac{d[SEAP](t)}{dt} = k_{transl,SEAP}\,[SEAP_{mRNA}]. \tag{1.2}$$

The Equations (1.1) and (1.2) are the full set of ODEs describing the model.

b. Implementation of the experiments and model simplifications.

The calibration of the model was performed using two distinct experiments, measuring the normalized SEAP production. These included a time-course experiment for up to 56 h and a tetO dose-response measurement with tetO concentrations of 1,2,3,4,5,6 and 26, i.e. a differing number of tetO DNA binding sites. Since in all experiments the normalized SEAP concentration was measured with the same methods, the Gaussian error parameters for the constant error sd_{abs} and the relative error sd_{rel} are the same for both experiments and are estimated jointly.

Experiment 1: Time course measurement of normalized SEAP production

We measured a SEAP production time course (TC) with values for 13 time-points from 0 h to 56 h after transfection of the cells with three replicates per measurements. The measurements were performed for both transcription factors TF- and TF+FUS. We normalized the SEAP production using the measured fluorescence of eYFP (i.e. the transcription factor concentration) as normalization factor. The observation function of the normalized SEAP is thus

$$\frac{SEAP_{observed}}{eYFP_{observed}} = scale_{ExperimentTC}[SEAP], \tag{1.3}$$

where $scale_{ExperimentTC}$ describes the scaling factor relating the normalized SEAP measurements to the state SEAP. This scaling factor is necessary to link the different measurement scales to the concentrations in the model. Since the absolute scale of the model state SEAP is unknown, one of these scaling parameters is fixed to an arbitrary value, removing the degree of freedom in the model linked to this arbitrary scaling and thus avoiding over-parametrization. We fixed

$$scale_{ExperimentTC} = 1. \tag{1.4}$$

Experiment 2: Dose-response measurements with varying amounts of tetO-repeats of normalized SEAP production

We measured a SEAP production dose response (DR) 52 h after transfection of the cells with three replicates per measurements. The measurements were performed for constructs with 1,2,3,4,5,6 and 26 tetO repeats for both transcription factors TF- and TF+FUS. We normalized the SEAP production using the measured fluorescence of eYFP (i.e. the transcription factor concentration) as normalization factor. The observation function of the normalized SEAP is

$$\frac{SEAP_{observed}}{eYFP_{observed}} = scale_{ExperimentDR}[SEAP]. \tag{1.5}$$

Initial Conditions

Solving the model equations requires initial conditions for the model states. They were set to

$$[SEAP](0) = 0 \quad \text{and} \tag{1.6}$$

$$[SEAP_{mRNA}](0) = 0 \tag{1.7}$$

because at the beginning of the measurements the cells were newly transfected and neither protein nor mRNA was yet produced.

Simplifications

The parameter $k_{transl,SEAP}$ describes the transition between $SEAP_{mRNA}$ and SEAP. However, since the absolute concentration of $SEAP_{mRNA}$ is unknown, it equates to a scaling factor linking the two concentrations. Thus, it can be fixed to

$$k_{transl,SEAP} = 1. \tag{1.8}$$

c. Results of the parameter estimation and uncertainty analysis

We performed the calibration of the model and the uncertainty analysis using a maximum likelihood approach. This approach is described in detail in Section (3) of this Supporting Information.

The model of the transcription factors TF- and TF+FUS was calibrated using 119 data points. The model includes 11 parameters, of which 10 are fitted and one is the fixed scaling parameter of the time-course experiment (see Equation (1.4)). The fitted parameters include one scaling parameter, two error parameters and seven dynamic parameters.

The entire analysis process was performed in MATLAB using the Data2Dynamics (48). software. The numerical integration of the ODEs within Data2Dynamics is performed using the CVODES solver (49). Parameter estimation uses the trust region algorithm LSQNONLIN (50). All parameters except the Hill coefficients h^* and the Michaelis-Menten constants K_m^* were optimized on a logarithmic scale to scan for the best parameters over many orders of magnitude.

Using 100 optimization runs with randomly sampled initial parameter sets, we searched for the optimal parameter set. 83 of the runs converged to the lowest minimum **(Modelling Fig. S1).** This suggests that this minimum is the global minimum and thus the globally optimal parameter set. The step like structure in **Modelling Fig. S1** suggests, that the optimization found one other minimum, however it is significantly worse than the best minimum.

We used the profile likelihood method to analyze the identifiably of the parameters and to quantify their uncertainty by calculating 95% confidence intervals. All parameters except for $k_{deg,SEAP}$ are identifiable **(Modelling Fig. S2)**. $k_{deg,SEAP}$ is practically non-identifiable and not significantly different from zero. This practical non-identifiability originates from the limited information available on the relatively slow degradation of SEAP mRNA in the experiments. A detailed list of the parameters and their uncertainties can be found in **Table S1**.

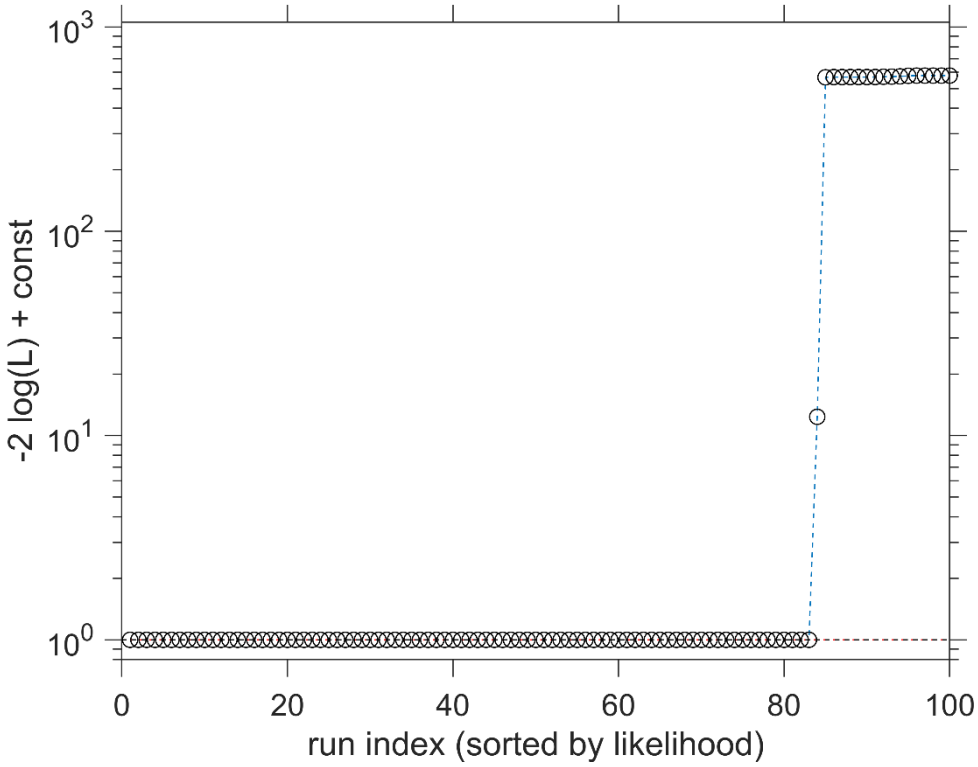

Modelling Fig. S1. Multiple optimization runs with random initial parameters for the model of TF- and TF+FUS. Multiple optimization runs with random initial parameter guesses for model of TF- and TF+FUS. We performed 100 optimization runs with random initial parameter guesses. Their results are sorted by their –2 log(L) value. 83 of the runs converged to the lowest minimum. All other local minima are significantly higher than this lowest minimum.

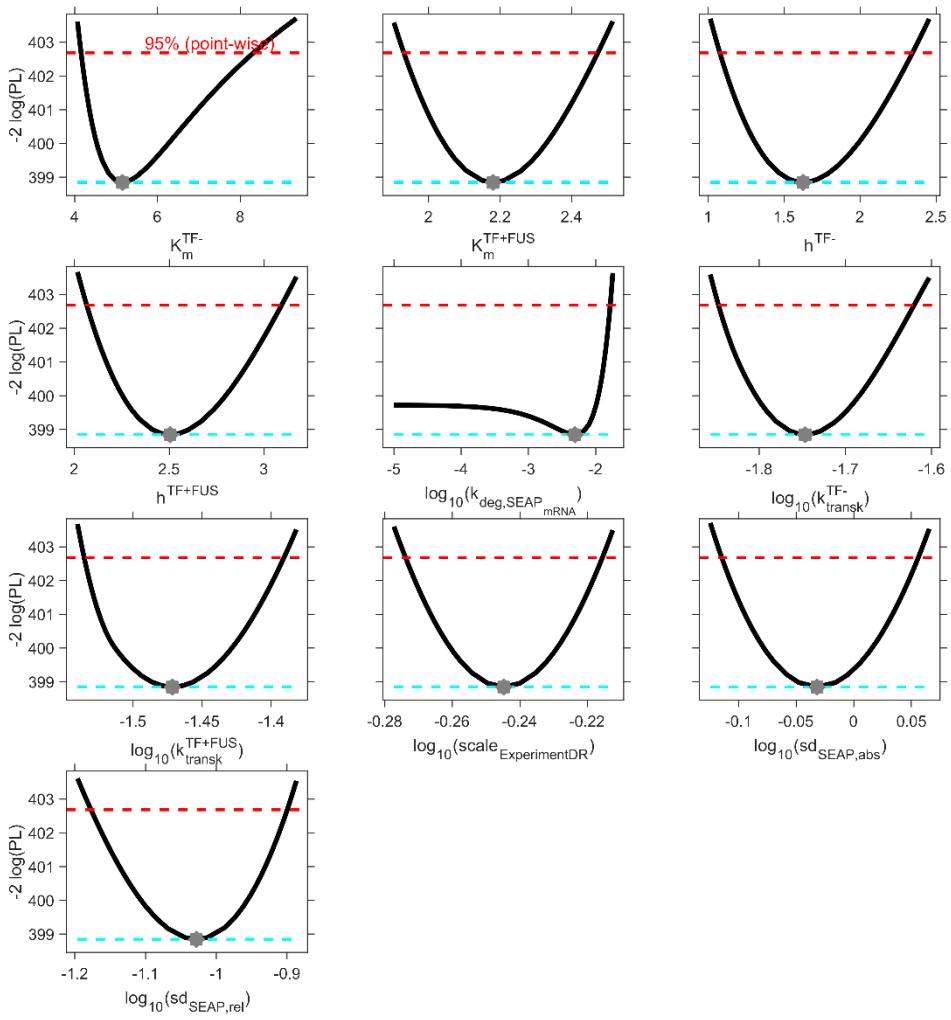

Modelling Fig. S2. Parameter profile likelihood of the estimated parameters for model of TF- and TF+FUS. Parameter profile likelihood of the estimated parameters of the model describing TF- and TF+FUS. The black lines show the profile likelihood, while the optimal parameter value, i.e. the Maximum Likelihood Estimator, is shown as a grey dot. The dashed red lines indicate the 95% confidence level. Its intersection points with the profile likelihood yield the point-wise 95% confidence intervals of the parameter. The dotted blue lines indicate the –2 log(PL) value of the optimal parameter set. All parameters are identifiable, i.e. they have finite 95% confidence intervals except for the practically non-identifiable parameter $k_{\text{deg,SEAP}}$.

Modelling Table S1. Estimated model parameters and confidence intervals based on parameter profile likelihood for the model of TF- and TF+FUS. Maximum likelihood estimation was used to obtain the estimated parameters $\hat{\theta}$. The point-wise 95% confidence intervals σ^- and σ^+ were obtained with the profile likelihood method. The fixed scaling parameter $\text{scale}_{\text{ExperimentTC}}$ has no confidence interval. The Michaelis-Menten constants K_m^* and the Hill parameters h^* were fitted on a linear scale, since they are naturally linearly confined.

Parameter	$\hat{\theta}$	σ^-	σ^+	Fitting scale
K_m^{TF-}	5.15	4.15	8.32	linear
K_m^{TF+FUS}	2.18	1.93	2.47	linear
h^{TF-}	1.62	1.08	2.34	linear
h^{TF+FUS}	2.50	2.07	3.09	linear
$k_{deg,SEAP_{mRNA}}$	$4.92 \cdot 10^{-03}$	$-\inf$	$1.65 \cdot 10^{-02}$	log10
k_{transk}^{TF-}	$1.79 \cdot 10^{-02}$	$1.42 \cdot 10^{-02}$	$2.40 \cdot 10^{-02}$	log10
k_{transk}^{TF+FUS}	$3.38 \cdot 10^{-02}$	$2.92 \cdot 10^{-02}$	$4.07 \cdot 10^{-02}$	log10
$scale_{ExperimentDR}$	$5.69 \cdot 10^{-01}$	$5.32 \cdot 10^{-01}$	$6.09 \cdot 10^{-01}$	log10
$scale_{ExperimentTC}$	$1.00 \cdot 10^{+00}$			not fitted
$sd_{SEAP,abs}$	$9.29 \cdot 10^{-01}$	$7.68 \cdot 10^{-01}$	$1.14 \cdot 10^{+00}$	log10
$sd_{SEAP,rel}$	$9.37 \cdot 10^{-02}$	$6.65 \cdot 10^{-02}$	$1.26 \cdot 10^{-01}$	log10

Section 2) Development of the extended mathematical model to describe DropletTFs and OptoDropletTFs.

a. Derivation of the set of ODEs.

In this chapter, we derive the extended mathematical model describing the TF-, TF+FUS and the OptoTF- and OptoTF+FUS transcription factors and the transcription of the reporter SEAP mRNA and translation of SEAP from its mRNA based on ODEs. This model is based on the previously introduced model in Section (1) of this SI.

However, since now a blue-light activation of the transcription has to be modelled, new model states are necessary. The photoreceptors Cry2(PHR)-eYFP-NLS-VP16 (OptoTF-) and Cry2(PHR)-eYFP-NLS-FUSn-VP16 (OptoTF+FUS) have a light-dependent transitioning behavior between their two respective conformations. In the dark, the Cry2 proteins are in their monomeric state while upon illumination with blue light with the intensity I_{blue} they oligomerize

$$[VP16_{\text{inactive}}] \underset{k_{\text{on,VP16}}\, I_{blue}}{\overset{k_{\text{off,VP16}}}{\rightleftarrows}} [VP16_{\text{active}}], \tag{2.1}$$

thus initiating the activation of the VP16 domain of the transcription factor from its inactive state $VP16_{\text{inactive}}$ to its active state $VP16_{\text{active}}$. This transition behavior only holds true for the optogenetic transcription factors OptoTF- and OptoTF+FUS. In the case of the other transcription factors TetR-VP16-NLS-eYFP (TF-) and TetR-VP16-NLS-FUSn-eYFP (TF+FUS), VP16 is always in its active state $VP16_{\text{active}}$. This was modelled with a Boolean variable b_{opto}, which is one for OptoTF- and OptoTF+FUS and zero for TF- and TF+FUS. The ODE describing the concentration of VP16 thus become

$$\frac{d[VP16_{\text{inactive}}](t)}{dt} = b_{opto}(-k_{\text{on,VP16}}\, I_{blue}[VP16_{\text{inactive}}] + k_{\text{off,VP16}}[VP16_{\text{active}}]) \tag{2.2}$$

and

$$\frac{d[VP16_{\text{active}}](t)}{dt} = b_{opto}(+k_{\text{on,VP16}}\, I_{blue}[VP16_{\text{inactive}}] - k_{\text{off,VP16}}[VP16_{\text{active}}]). \tag{2.3}$$

As in the previous model, the transcription factors binding to the tetO sites lead to the transcription of $SEAP_{mRNA}$ which in turn invokes the production of the reporter protein SEAP. The modelling is again performed using a Hill reaction, described in Equation (1.1) with the reaction rate k^*_{transk} and the Michaelis-Menten constant K^*_m, as well as the Hill parameter h^*. These three parameters were fitted separately for each transcription factor. The degradation rate of $SEAP_{mRNA}$ $k_{deg,SEAP}$ however, is the same for all four transcription factors. In contrast to Equation (1.1), now, the linear activation of mRNA transcription by the transcription factors is modelled by introducing the VP16-based transcription. The equation thus becomes

$$\frac{d[SEAP_{mRNA}](t)}{dt} = \frac{k^*_{transk}\,[tetO]^{h^*}}{(K^*_m)^{h^*} + [tetO]^{h^*}}[VP16_{\text{active}}]^{h_{VP16}} - k_{deg,SEAP}\,[SEAP_{mRNA}]. \quad (2.4)$$

Here, the cooperativity of the VP16 induced transcription activation is modelled by the Hill parameter h_{VP16}.

The translation of SEAP by $SEAP_{mRNA}$

$$\frac{d[SEAP](t)}{dt} = k_{transl,SEAP}\,[SEAP_{mRNA}] \quad (2.5)$$

is identical to Equation (1.2). Thus, Equations (2.2) – (2.5) are able to describe the extended system of both TF-, TF+FUS as well as OptoTF- and OptoTF+FUS.

b. Implementation of the extended experiments and model simplifications.

Experiments 1 and 2: Time course measurement of normalized SEAP production and tetO dose-response measurements of TF- and TF+FUS

Since this model is an extension of the previously defined model, the two experiments discussed in Section 1 describing the time courses (TC) of TF- and TF+FUS as well as their tetO-dose responses (DR) are also included in this model. Their observation functions are defined by

$$\frac{SEAP_{observed}}{eYFP_{observed}} = scale_{ExperimentTC}[SEAP] \quad (2.6)$$

and

$$\frac{SEAP_{observed}}{eYFP_{observed}} = scale_{ExperimentDR}[SEAP] \quad (2.7)$$

identically to Equations (1.3) and (1.5). Again, one of the scaling factors linking the normalized SEAP measurements to the concentration of SEAP in the model can be fixed. We used the scale of the time course measurement

$$scale_{ExperimentTC} = 1. \quad (2.8)$$

and set it to one as we also did for the smaller model in Equation (1.4).

Experiment 3: Time course measurement of normalized SEAP production of OptoTF- and OptoTF+FUS

We kept the cells which were transfected with OptoTF- and OptoTF+FUS in darkness for 24 h in order to be able to transcribe and translate the transcription factor components necessary for the experiment. Since the transcription factor components including Cry2 are inactive in darkness, we started our measurements upon

illuminating the cells with blue light (465 nm, 5 µmol m^{-2} s^{-1}). We then measured SEAP production values for 8 time-points from 0 h to 32 h after starting the illumination with three replicates per measurements. The measurements were performed for both transcription factors OptoTF- and OptoTF+FUS. We normalized the SEAP production using the measured fluorescence of eYFP as normalization factor. The observation function of the normalized SEAP is thus similar to the time course measurement of experiment 1

$$\frac{SEAP_{observed}}{eYFP_{observed}} = scale_{ExperimentTC,Opto}[SEAP], \tag{2.9}$$

where $scale_{ExperimentTC\_Opto}$ describes the scaling factor relating the normalized SEAP measurements to the state SEAP. Since the absolute scale of the model state SEAP for the optogenetic conditions of the model is unknown, one of the scaling parameters from the measurements of the optogenetic system has to be fixed to an arbitrary value, too. This removes the degree of freedom in the model linked to this arbitrary scaling and thus avoids over-parametrization. We fixed

$$scale_{ExperimentTC,Opto} = 1. \tag{2.10}$$

Experiment 4: Dose response measurements with varying amounts of tetO-repeats of normalized SEAP production of OptoTF- and OptoTF+FUS

The dose-response measurement of the optogenetic transcription factors was performed similarly to the time course experiment, i.e. the cells were kept in the dark for 24 h first. Afterwards, they were kept under blue light. We measured SEAP production values 52 h after starting the illumination of the cells with three replicates per measurements. The measurements were performed for constructs with 1,2,3,4,5,6 and 26 tetO repeats for both transcription factors OptoTF- and OptoTF+FUS. We normalized the SEAP production levels as previously discussed. The observation function of the normalized SEAP is

$$\frac{SEAP_{observed}}{eYFP_{observed}} = scale_{ExperimentDR,Opto}[SEAP]. \tag{2.11}$$

Initial Conditions

Solving the model equations requires initial conditions for the model states. For SEAP and its mRNA they were set to

$$[SEAP](0) = 0 \quad \text{and} \tag{2.12}$$

$$[SEAP_{mRNA}](0) = 0. \tag{2.13}$$

These initial conditions are true for all transcription factors. For the TF- and TF+FUS transcription factors this is because at the beginning of the measurements, cells were newly transfected and therefore had not yet produced neither mRNA nor protein. For

OptoTF- and OptoTF+FUS the cells were kept in the dark for 24h after transfection, thus no SEAP mRNA or protein was produced.

Since the scaling of the VP16 states can be arbitrarily chosen by the model, we choose initial conditions that ensured that for all conditions the active state of VP16 had the same concentration of one. This makes the comparison of the model parameters between the OptoTF and TF systems possible. Thus, the initial conditions for the TF system are

$$[VP16_{\text{active}}](0) = 1 \quad \text{and} \tag{2.14}$$

$$[VP16_{\text{inactive}}](0) = 0 \tag{2.15}$$

For the OptoTF system the initial conditions are determined by the steady state of the two VP16 states, which is dependent on the blue light intensity I_{blue} as well as the rates of the VP16 reactions $k_{\text{on,VP16}}$ and $k_{\text{off,VP16}}$. They are

$$[VP16_{\text{active}}](0) = 1 \quad \text{and} \tag{2.16}$$

$$[VP16_{\text{inactive}}](0) = \frac{k_{\text{off,VP16}}}{I_{blue}\, k_{\text{on,VP16}}}. \tag{2.17}$$

The total concentration of VP16 is conserved in the model.

Simplifications

The parameter $k_{transl,SEAP}$ describes the transition between $SEAP_{mRNA}$ and SEAP. As discussed for the smaller model, since the absolute concentration of $SEAP_{mRNA}$ is unkown, it equates to a scaling factor linking the two concentrations and can be fixed to one (Equation (1.8)).

The values of the parameters describing the blue light-dependent activation of the VP16 transcription factors, i.e. the conformational change of Cry2 were fixed to previously determined values. The dark revision of activated Cry2 happens with the half-life of 5.5 min (51), thus the rate describing the dark revision can be fixed by

$$k_{\text{off,VP16}} = \frac{1}{5.5}[\text{min}^{-1}] = \frac{60}{5.5}[\text{h}^{-1}]. \tag{2.18}$$

The activation rate of a similar optogenetic transcription factor was determined (52) to be

$$k_{\text{on,VP16}} = 5.0 \text{ x } 10^{-2}\ [(\text{h}\ \mu\text{mol m}^{-2}\ \text{s}^{-2})^{-1}]\,. \tag{2.19}$$

Furthermore, the Hill parameter of the VP16 activation h_{VP16} cannot be determined from the given measurements. In order to estimate this parameter, multiple blue-light intensities have to be measured thus leading to differing concentrations of $VP16_{\text{active}}$. Therefore, the parameter was fixed

$$h_{VP16} = 2, \quad (2.20)$$

assuming cooperativity in Cry2 oligomerization.

c. Results of the parameter estimation and uncertainty analysis of the extended model.

We performed the calibration of the model and the uncertainty analysis using a maximum likelihood approach. This approach is described in detail in Section (3) of this Supporting Information.
The extended model of the transcription factors TF-, TF+FUS, OptoTF- and OptoTF+FUS was calibrated using 209 data points. The model includes 22 parameters, of which 17 are fitted, two are fixed scaling parameters of the time-course experiments (see Equations (2.8) and (2.10)), two are the fixed rates of VP16 and one is the fixed Hill parameter of the same compound. The fitted parameters include two scaling parameters, two error parameters and thirteen dynamic parameters.
The entire analysis process was performed in MATLAB using the Data2Dynamics[10] software. The numerical integration of the ODEs within Data2Dynamics is performed using the CVODES solver (49). Parameter estimation uses the trust region algorithm LSQNONLIN (50). All parameters except the Hill coefficients and the Michaelis-Menten constants K_m^* were optimized on a logarithmic scale to scan for the best parameters over many orders of magnitude.

Using 100 optimization runs with randomly sampled initial parameter sets, we searched for the optimal parameter set. 91 of the runs converged to the lowest minimum **(Modelling Fig. S3)**. This suggests that this minimum is the global minimum and thus the globally optimal parameter set. The step-like structure in **Modelling Fig. S3** suggests, that the optimization found other minima, however they are significantly worse than the best minimum.
We used the profile likelihood method to analyze the identifiably of the parameters and to quantify their uncertainty by calculating 95% confidence intervals. All parameters are identifiable **(Modelling Fig. S4)**. $k_{deg,SEAP}$, which was practically non-identifiable in the smaller model now is also identifiable. This suggests that the combined information from all four experiments sufficiently restricts the uncertainty of the parameter in order to become identifiable. A detailed list of the parameters and their uncertainties can be found in **Modelling Table S2**.

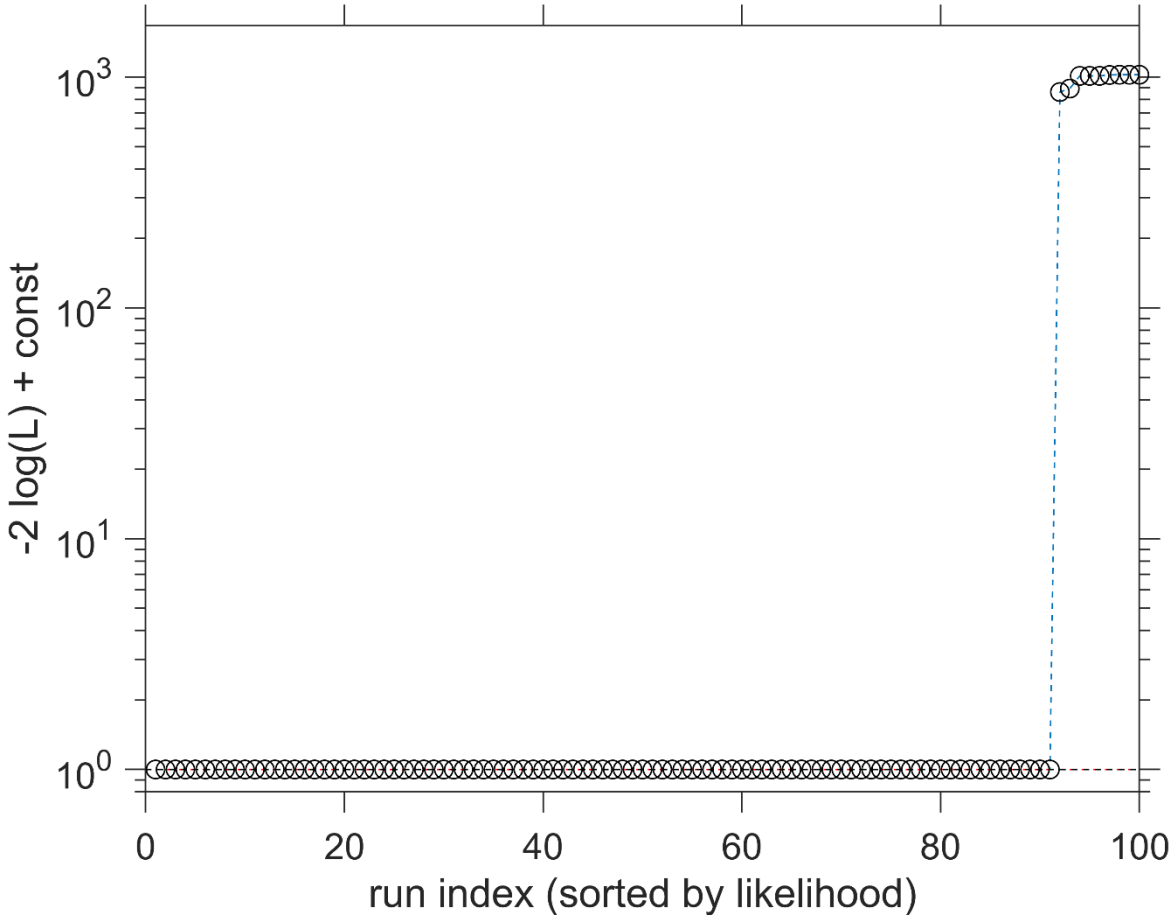

Modelling Fig. S3. Multiple optimization runs with random initial parameters for extended model of TF-, TF+FUS, OptoTF- and OptoTF+FUS. Multiple optimization runs with random initial parameter guesses for model of TF- and TF+FUS. We performed 100 optimization runs with random initial parameter guesses. Their results are sorted by their –2 log(L) value. 91 of the runs converged to the lowest minimum. All other local minima are significantly higher than this lowest minimum.

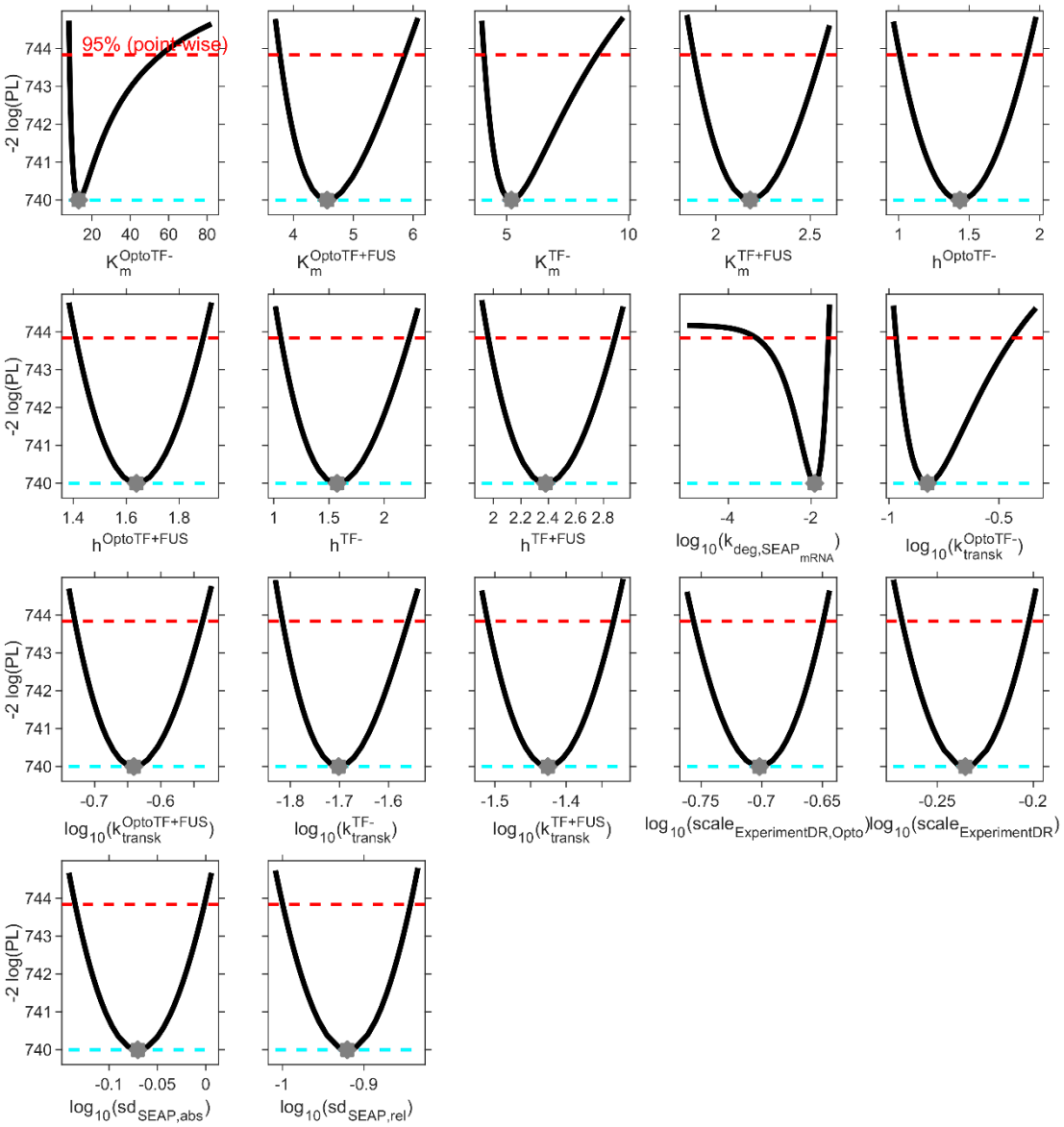

Modelling Fig. S4. **Parameter profile likelihood of the estimated parameters for extended model of TF-, TF+FUS, OptoTF- and OptoTF+FUS.** Parameter profile likelihood of the estimated parameters of model describing TF-, TF+FUS, OptoTF- and OptoTF+FUS. The black lines show the profile likelihood, while the optimal parameter value, i.e. the Maximum Likelihood Estimator, is shown as a grey dot. The dashed red lines indicate the 95% confidence level. Its intersection points with the profile likelihood yield the point-wise 95% confidence intervals of the parameter. The dotted blue lines indicate the –2 log(PL) value of the optimal parameter set. All parameters are identifiable.

Modelling Table S2. Estimated model parameters and confidence intervals based on parameter profile likelihood for the extended model of TF-, TF+FUS, OptoTF- and OptoTF+FUS. Maximum likelihood estimation was used to obtain the

estimated parameters $\hat{\theta}$. The point-wise 95% confidence intervals σ^- and σ^+ were obtained with the profile likelihood method. The fixed scaling parameters $\text{scale}_{\text{ExperimentTC}}$ and $\text{scale}_{\text{ExperimentTC,Opto}}$ as well as the fixed parameters $k_{\text{off,VP16}}$, $k_{\text{on,VP16}}$, and h_{VP16} have no confidence intervals. The Michaelis-Menten constants K_m^* and the Hill parameters h^* were fitted on a linear scale, since they are naturally linearly confined.

Parameter	$\hat{\theta}$	σ^-	σ^+	log10
$K_m^{OptoTF-}$	13.1	8.26	56.1	linear
$K_m^{OptoTF+FUS}$	4.56	3.77	5.86	linear
K_m^{TF-}	5.20	4.07	8.70	linear
K_m^{TF+FUS}	2.18	1.88	2.56	linear
h_{VP16}	2.00			not fitted
$h^{OptoTF-}$	1.43	1.01	1.91	linear
$h^{OptoTF+FUS}$	1.64	1.41	1.89	linear
h^{TF-}	1.57	1.06	2.23	linear
h^{TF+FUS}	2.38	1.96	2.88	linear
$k_{deg,SEAP_{mRNA}}$	$1.23 \cdot 10^{-02}$	$4.76 \cdot 10^{-04}$	$2.63 \cdot 10^{-02}$	log10
$k_{off,VP16}$	$1.09 \cdot 10^{+01}$			not fitted
$k_{on,VP16}$	$5.00 \cdot 10^{-02}$			not fitted
$k_{transk}^{OptoTF-}$	$1.50 \cdot 10^{-01}$	$1.08 \cdot 10^{-01}$	$3.65 \cdot 10^{-01}$	log10
$k_{transk}^{OptoTF+FUS}$	$2.29 \cdot 10^{-01}$	$1.86 \cdot 10^{-01}$	$2.90 \cdot 10^{-01}$	log10
k_{transk}^{TF-}	$1.99 \cdot 10^{-02}$	$1.53 \cdot 10^{-02}$	$2.75 \cdot 10^{-02}$	log10
k_{transk}^{TF+FUS}	$3.75 \cdot 10^{-02}$	$3.09 \cdot 10^{-02}$	$4.64 \cdot 10^{-02}$	log10
$scale_{ExperimentDR,Opto}$	$1.99 \cdot 10^{-01}$	$1.75 \cdot 10^{-01}$	$2.24 \cdot 10^{-01}$	log10
$scale_{ExperimentDR}$	$5.82 \cdot 10^{-01}$	$5.39 \cdot 10^{-01}$	$6.28 \cdot 10^{-01}$	log10
$scale_{ExperimentTC}$	1.00			not fitted
$scale_{ExperimentTC,Opto}$	1.00			not fitted
$sd_{SEAP,abs}$	$8.50 \cdot 10^{-01}$	$7.32 \cdot 10^{-01}$	$9.97 \cdot 10^{-01}$	log10
$sd_{SEAP,rel}$	$1.20 \cdot 10^{-01}$	$1.00 \cdot 10^{-01}$	$1.44 \cdot 10^{-01}$	log10

d. Model prediction of blue-light dose-response measurement.

The predictions of the aforementioned calibrated model suggest that the OptoTF+FUS system reaches higher gene expression levels than the OptoTF- system, even for lower light intensities than the 5 µmol m^{-2} s^{-1} used in the experiments for the calibration of the model. For testing this prediction we measured the SEAP production of OptoTF- and OptoTF+FUS for varying intensities of blue light (465 nm, 0.1, 0.17, 0.32, 0.5 µmol m^{-2} s^{-1}) 48 h after transfection.

The observation function of the newly measured dataset is described by

$$\frac{SEAP_{observed}}{eYFP_{observed}} = scale_{Validation,LightDR}[SEAP]. \quad (2.21)$$

Determining the uncertainties of the model prediction for these measurement conditions requires fitting the newly measured data in order to determine the inherent scaling factor $scale_{Validation,LightDR}$ of the data. Furthermore, since in contrast to the calibrated model for all four transcription factors **(SI Modelling Section 2 c)** now the VP16 concentrations differ due to different light intensities, the Hill parameter h_{VP16} has to be fitted to the new dataset as well. This fitting process is performed using the fixed maximum likelihood estimate for all other parameters of the previously calibrated model. We used the profile likelihood method to determine the uncertainty of the two parameters and their identifiability **(Modelling Fig. S5)**. Both parameters are identifiable. Their detailed list can be found in **Modelling Table S3**.

Using these two parameters, the uncertainty of the model prediction for the given experimental conditions, i.e. the blue-light dose response of OptoTF- and OptoTF+FUS can be calculated. For this purpose, the prediction profile likelihood (37, 55) of the respective conditions was calculated. For this uncertainty, however, only the four experimental datasets of the original model can be used. The light-dose response dataset cannot be used for this prediction if it is to be compared to the predicted trajectories. Nevertheless, the uncertainty of the estimation of the scaling and Hill parameter has to be propagated to the model prediction. They were included in the model by introducing a log-normal prior $N(\mu, \sigma_N^2)$ with a standard deviation of

$$\sigma_N = 3.84 \text{ x } (\sigma^+ - \sigma^-), \quad (2.22)$$

where σ^+ and σ^- describe point-wise confidence intervals of the parameter, and the mean

$$\mu = \hat{\theta}, \quad (2.23)$$

i.e. the maximum likelihood estimate of the previous calibration process to the parameters $scale_{Validation,LightDR}$ and h_{VP16}. These priors ensure that the profile likelihood of the parameters is identical to the profile likelihood of the calibration model **(Modelling Fig. S5)**. The adjustment of the prior by 3.84 is necessary to adjust the size of the 95% confidence intervals to the width of the log-normal prior.

Given the uncertainty of the extended model as well as the propagated uncertainty of the coupling of the data with the model via scaling and Hill kinetics, the prediction profile likelihood yields a predicted model trajectory as well as the uncertainty of this prediction **(Figure 4 b)**. The measured data is in agreement with these trajectories suggesting that OptoTF+FUS indeed yields higher SEAP production for identical blue-light intensities when compared to OptoTF-.

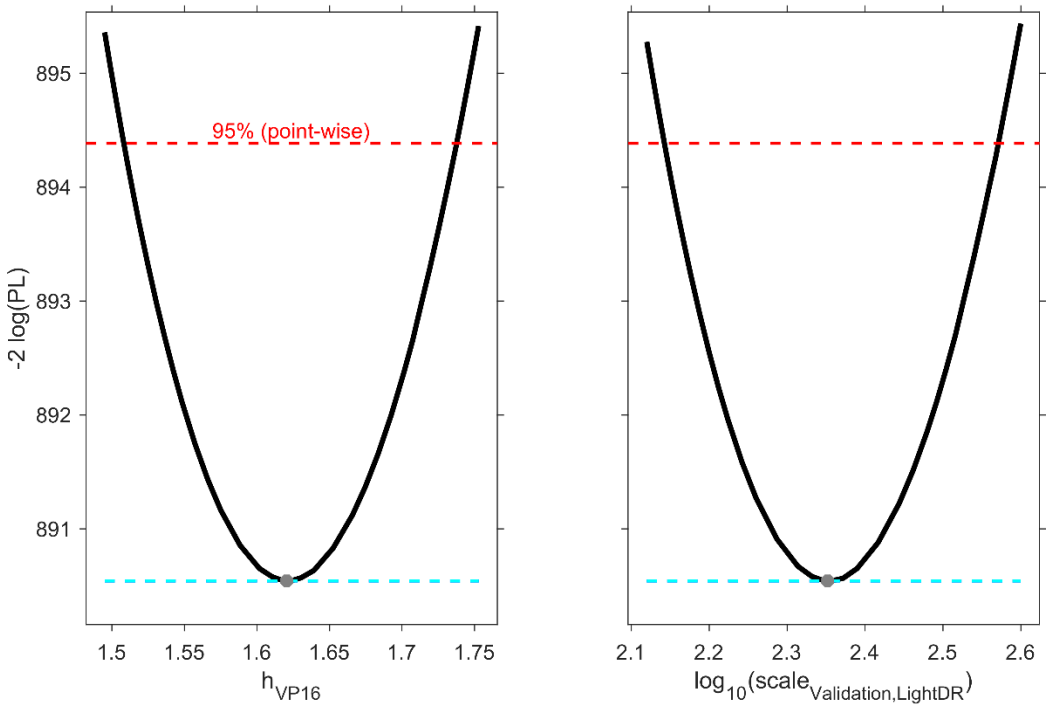

Modelling Fig. S5. **Parameter profile likelihood of the estimated parameters for the extended model of TF-, TF+FUS, OptoTF- and OptoTF+FUS including the light-dose response dataset.** Parameter profile likelihood of the two estimated parameters of model including the extended light-dose response dataset. The black lines show the profile likelihood, while the optimal parameter value, i.e. the Maximum Likelihood Estimator, is shown as a grey dot. The dashed red lines indicate the 95% confidence level. Its intersection points with the profile likelihood yield the point-wise 95% confidence intervals of the parameter. The dotted blue lines indicate the –2 log(PL) value of the optimal parameter set. Both parameters are identifiable. All other parameters of the model were fixed to the maximum likelihood estimate of the extended model **(Modelling Table S2)**.

Modelling Table S3. Estimated model parameters and confidence intervals based on parameter profile likelihood for the extended model of TF-, TF+FUS, OptoTF- and OptoTF+FUS including the light-dose response dataset. Maximum likelihood estimation was used to obtain the estimated parameters $\hat{\theta}$. The point-wise 95% confidence intervals σ^- and σ^+ were obtained with the profile likelihood method. All other parameters were fixed to the maximum likelihood estimate of the extended model **(Modelling Table S2)**.

Parameter	$\hat{\theta}$	σ^-	σ^+	log10
h_{VP16}	1.62	1.51	1.74	linear
$scale_{Validation,LightDR}$	$2.25 \cdot 10^{+02}$	$1.39 \cdot 10^{+02}$	$3.73 \cdot 10^{+02}$	log10

Section 3) Introduction to the maximum likelihood approach to parametrize the models and perform identifiably analysis.

We developed two mathematical models based on ordinary differential equations (ODEs). Their detailed derivation can be found in the preceding sections. For the parametrization of these models we used a maximum likelihood approach. For the uncertainty analysis we used the profile likelihood method. These methods will be introduced here briefly, based on previous introductions in Raue et. al. (53) and the supporting information of Beyer et al. (54).

The mathematical models discussed in this work describe the dynamics of the concentrations of the relevant biochemical complexes. Using $\vec{x}$ as the vector of these states, the ODEs can be generalized to

$$\frac{d}{dt}\vec{x}(t) = \vec{f}\left(\vec{x}, \vec{p}, \vec{u}(t)\right), \tag{3.1}$$

where $\vec{p}$ describes the vector of dynamic variables and $\vec{u}(t)$ the time dependent external inputs. Solving these ODEs requires initial values for the vector $\vec{x}$ at t = 0, which can either be estimated or be fixed to a specific value.
Measurements of specific concentrations within cells directly is impossible, thus, no direct measurements of the states $\vec{x}$ are available. Therefore, an observation function

$$y(t) = g(\vec{x}(t), \vec{s}) + \vec{\varepsilon}(t) \tag{3.2}$$

has to be used to link the measurements $y(t)$ to the states $\vec{x}(t)$. This observation function g includes observation parameters $\vec{s}$, e.g. scaling factors of the measurement. The error model of the observations is encoded in the noise term $\vec{\varepsilon}(t)$. We used the error model

$$\varepsilon = \varepsilon_{abs} + \varepsilon_{rel}. \tag{3.3}$$

$\varepsilon_{abs} \sim N(0, \sigma_{abs}^2)$ describes a constant Gaussian error with variance σ_{abs}^2, while $\varepsilon_{rel} \sim N\left(0, \sigma_{rel}^2\, g(\vec{x}(t), \vec{s})\right)$ describes a Gaussian error with a variance relative to the simulated state in g scaled by σ_{rel}^2. Thus, the total variance σ^2 at the time point t_j becomes

$$\sigma_j \left(g\left(\vec{x}(t_j), \vec{s}\right)\right)^2 = \sigma_{abs}^2 + \sigma_{rel}^2\; g\left(\vec{x}(t_j), \vec{s}\right). \tag{3.4}$$

Given N_D data points of one experiment with the measurement vector $\vec{y}^D$, the probability of these measurements given a specific set of parameters $\vec{\theta} = (\vec{p}, \vec{x}_0, \vec{s}, \sigma)$ can be defined as

$$L\left(\vec{y}^D, \vec{\theta}\right) = \frac{1}{\sqrt{2\pi\sigma_j \left(g\left(\vec{x}(t_j), \vec{s}\right)\right)^2}} \prod_{j=1}^{N_D} exp\left(\frac{\left(y_j^D - g\left(\vec{x}(t_j), \vec{s}\right)\right)^2}{2\sigma_j \left(g\left(\vec{x}(t_j), \vec{s}\right)\right)^2}\right), \tag{3.5}$$

where t_j denotes the time of the measurement y_j^D. These parameters include the ODE parameters $\vec{p}$, estimated initial concentrations $\vec{x}_0$, observable parameters $\vec{s}$, and the

error parameters σ. In general, multiple experiments, i.e. measurements $\vec{y}^D$ with distinct observation functions g are used to calibrate the model. A general term for the likelihood function using N_{exp} experiments is

$$L(\vec{y}^D, \vec{\theta}) = \prod_{k=1}^{N_{exp}} L(\vec{y}^{D_k}, \vec{\theta}_k). \tag{3.6}$$

The maximum likelihood estimator

$$\hat{\theta} = \underset{\theta}{\operatorname{argmax}} \left(L(\vec{y}^D, \vec{\theta}) \right). \tag{3.7}$$

gives the parameter set $\hat{\theta}$, for which the measurements are most likely, i.e. have the highest probability. Instead of maximizing the likelihood without any loss of generality $\chi^2_{mod}(\vec{\theta}, \vec{y}^D) := -2\log(L)$ can be minimized. For the Gaussian distributed errors this term

$$\chi^2_{mod}(\vec{\theta}, \vec{y}^D) = \underbrace{\sum_{j=1}^{N_D} \left(\frac{\left(y_j^D - g(\vec{x}(t_j), \vec{s}) \right)^2}{2{\sigma_j}^2} \right)}_{\chi^2(\vec{\theta}, \vec{y}^D)} + \underbrace{\sum_{j=1}^{N_D} \left(2\, N_D\, log\left(\sqrt{2\pi\, {\sigma_j}^2} \right) \right)}_{\rho(\vec{\theta})} \tag{3.8}$$

consists of the sum of the square of the residuals of the data $\chi^2(\vec{\theta}, \vec{y}^D)$ as well a an error correction term $\rho(\vec{\theta})$ independent of the data.

After calibrating the model to $\hat{\theta}$, a major question remains about the uncertainty of the parameters in the non-linear context of the model. We performed an uncertainty analysis of the model as well as an identifiability analysis of the parameters using the profile likelihood method (55). It gives finite sample likelihood based intervals by using a threshold in the likelihood. The profile likelihood

$$\chi^2_{PL}(\theta_i) = \min_{\theta_{i \neq j}} \left(\chi^2_{mod}(\vec{\theta}, \vec{y}^D) \right) \tag{3.9}$$

of the parameter θ_i thus encodes the path with the highest likelihood along the parameter axis. This translates into a 95% confidence interval (CI) of the parameter

$$CI(\theta_i) = \left\{ \theta \middle| \, \chi^2_{PL}(\theta) - \chi^2_{PL}(\vec{\theta}) < \chi^2(95\%, df = 1) \right\}, \tag{3.10}$$

where $\chi^2(95\%, df = 1)$ is the 95th quantile of the χ^2- distribution with one degree of freedom.

REFERENCES AND NOTES

1. M. Mansouri, T. Strittmatter, M. Fussenegger, Light-controlled mammalian cells and their therapeutic applications in synthetic biology. *Adv. Sci. (Weinh)* **6**, 1800952 (2019).

2. J. Hartmann, D. Krueger, S. De Renzis, Using optogenetics to tackle systems-level questions of multicellular morphogenesis. *Curr. Opin. Cell Biol.* **66**, 19–27 (2020).

3. D. Krueger, E. Izquierdo, R. Viswanathan, J. Hartmann, C. P. Cartes, S. de Renzis, Principles and applications of optogenetics in developmental biology. *Development* **146**, dev175067 (2019).

4. H. Ye, M. D.-E. Baba, R.-W. Peng, M. Fussenegger, A synthetic optogenetic transcription device enhances blood-glucose homeostasis in mice. *Science* **332**, 1565–1568 (2011).

5. K. Kolar, W. Weber, Synthetic biological approaches to optogenetically control cell signaling. *Curr. Opin. Biotechnol.* **47**, 112–119 (2017).

6. K. Kolar, C. Knobloch, H. Stork, M. Žnidarič, W. Weber, OptoBase: A web platform for molecular optogenetics. *ACS Synth. Biol.* **7**, 1825–1828 (2018).

7. A. A. Kaberniuk, A. A. Shemetov, V. V. Verkhusha, A bacterial phytochrome-based optogenetic system controllable with near-infrared light. *Nat. Methods* **13**, 591–597 (2016).

8. C. P. Brangwynne, C. R. Eckmann, D. S. Courson, A. Rybarska, C. Hoege, J. Gharakhani, F. Jülicher, A. A. Hyman, Germline P granules are liquid droplets that localize by controlled dissolution/condensation. *Science* **324**, 1729–1732 (2009).

9. J. A. Riback, C. D. Katanski, J. L. Kear-Scott, E. V. Pilipenko, A. E. Rojek, T. R. Sosnick, D. A. Drummond, Stress-triggered phase separation is an adaptive, evolutionarily tuned response. *Cell* **168**, 1028–1040.e19 (2017).

10. M. Prouteau, R. Loewith, Regulation of cellular metabolism through phase separation of enzymes. *Biomolecules.* **8**, 160 (2018).

11. X. Su, J. A. Ditlev, E. Hui, W. Xing, S. Banjade, J. Okrut, D. S. King, J. Taunton, M. K. Rosen, R. D. Vale, Phase separation of signaling molecules promotes T cell receptor signal transduction. *Science* **352**, 595–599 (2016).

12. L. B. Case, X. Zhang, J. A. Ditlev, M. K. Rosen, Stoichiometry controls activity of phase-separated clusters of actin signaling proteins. *Science* **363**, 1093–1097 (2019).

13. J. Sheu-Gruttadauria, I. J. MacRae, Phase transitions in the assembly and function of human miRISC. *Cell* **173**, 946–957.e16 (2018).

14. E. M. Langdon, A. S. Gladfelter, A new lens for RNA localization: Liquid-liquid phase separation. *Annu. Rev. Microbiol.* **72**, 255–271 (2018).

15. H. B. Schmidt, D. Görlich, Transport selectivity of nuclear pores, phase separation, and membraneless organelles. *Trends Biochem. Sci.* **41**, 46–61 (2016).

16. A. S. Holehouse, R. V. Pappu, Functional implications of intracellular phase transitions. *Biochemistry* **57**, 2415–2423 (2018).

17. Y. Shin, C. P. Brangwynne, Liquid phase condensation in cell physiology and disease. *Science* **357**, eaaf4382 (2017).

18. S. F. Banani, H. O. Lee, A. A. Hyman, M. K. Rosen, Biomolecular condensates: Organizers of cellular biochemistry. *Nat. Rev. Mol. Cell Biol.* **18**, 285–298 (2017).

19. A. R. Strom, C. P. Brangwynne, The liquid nucleome–phase transitions in the nucleus at a glance. *J. Cell Sci.* **132**, jcs235093 (2019).

20. M. Feric, N. Vaidya, T. S. Harmon, D. M. Mitrea, L. Zhu, T. M. Richardson, R. W. Kriwacki, R. V. Pappu, C. P. Brangwynne, Coexisting liquid phases underlie nucleolar subcompartments. *Cell* **165**, 1686–1697 (2016).

21. D. Hnisz, K. Shrinivas, R. A. Young, A. K. Chakraborty, P. A. Sharp, A phase separation model for transcriptional control. *Cell* **169**, 13–23 (2017).

22. I. I. Cisse, I. Izeddin, S. Z. Causse, L. Boudarene, A. Senecal, L. Muresan, C. Dugast-Darzacq, B. Hajj, M. Dahan, X. Darzacq, Real-time dynamics of RNA polymerase II clustering in live human cells. *Science* **341**, 664–667 (2013).

23. W.-K. Cho, J.-H. Spille, M. Hecht, C. Lee, C. Li, V. Grube, I. I. Cisse, Mediator and RNA polymerase II clusters associate in transcription-dependent condensates. *Science* **361**, 412–415 (2018)

24. A. Boija, I. A. Klein, B. R. Sabari, A. Dall'Agnese, E. L. Coffey, A. V. Zamudio, C. H. Li, K. Shrinivas, J. C. Manteiga, N. M. Hannett, B. J. Abraham, L. K. Afeyan, Y. E. Guo, J. K. Rimel, C. B. Fant, J. Schuijers, T. I. Lee, D. J. Taatjes, R. A. Young, Transcription factors activate genes through the phase-separation capacity of their activation domains. *Cell* **175**, 1842–1855.e16 (2018).

25. B. R. Sabari, A. Dall'Agnese, A. Boija, I. A. Klein, E. L. Coffey, K. Shrinivas, B. J. Abraham, N. M. Hannett, A. V. Zamudio, J. C. Manteiga, C. H. Li, Y. E. Guo, D. S. Day, J. Schuijers, E. Vasile, S. Malik, D. Hnisz, T. I. Lee, I. I. Cisse, R. G. Roeder, P. A. Sharp, A. K. Chakraborty, R. A. Young, Coactivator condensation at super-enhancers links phase separation and gene control. *Science* **361**, eaar3958 (2018).

26. M. Boehning, C. Dugast-Darzacq, M. Rankovic, A. S. Hansen, T. Yu, H. Marie-Nelly, D. T. McSwiggen, G. Kokic, G. M. Dailey, P. Cramer, X. Darzacq, M. Zweckstetter, RNA polymerase II clustering through carboxy-terminal domain phase separation. *Nat. Struct. Mol. Biol.* **25**, 833–840 (2018).

27. M. Gossen, H. Bujard, Tight control of gene expression in mammalian cells by tetracycline-responsive promoters. *Proc. Natl. Acad. Sci. U.S.A.* **89**, 5547–5551 (1992).

28. Y. Lin, S. L. Currie, M. K. Rosen, Intrinsically disordered sequences enable modulation of protein phase separation through distributed tyrosine motifs. *J. Biol. Chem.* **292**, 19110–19120 (2017).

29. J. Berger, J. Hauber, R. Hauber, R. Geiger, B. R. Cullen, Secreted placental alkaline phosphatase: A powerful new quantitative indicator of gene expression in eukaryotic cells. *Gene* **66**, 1–10 (1988).

30. G. Sitton, A. Hansgate, F. Srienc, Transient gene expression in CHO cells monitored with automated flow cytometry. *Cytotechnology* **52**, 13–24 (2006).

31. S. Schlatter, M. Rimann, J. Kelm, M. Fussenegger, *SAMY*, a novel mammalian reporter gene derived from *Bacillus stearothermophilus* α-amylase. *Gene* **282**, 19–31 (2002).

32. Y. Shin, J. Berry, N. Pannucci, M. P. Haataja, J. E. Toettcher, C. P. Brangwynne, Spatiotemporal control of intracellular phase transitions using light-activated optoDroplets. *Cell* **168**, 159–171.e14 (2017).

33. A. Rademacher, F. Erdel, J. Trojanowski, S. Schumacher, K. Rippe, Real-time observation of light-controlled transcription in living cells. *J. Cell Sci.* **130**, 4213–4224 (2017).

34. D. L. Che, L. Duan, K. Zhang, B. Cui, The dual characteristics of light-induced cryptochrome 2, homo-oligomerization and heterodimerization, for optogenetic manipulation in mammalian cells. *ACS Synth. Biol.* **4**, 1124–1135 (2015).

35. S. M. Janicki, T. Tsukamoto, S. E. Salghetti, W. P. Tansey, R. Sachidanandam, K. V. Prasanth, T. Ried, Y. Shav-Tal, E. Bertrand, R. H. Singer, D. L. Spector, From silencing to gene expression: Real-time analysis in single cells. *Cell* **116**, 683–698 (2004).

36. N. Riggi, L. Cironi, M. L. Suvà, I. Stamenkovic, Sarcomas: Genetics, signalling, and cellular origins. Part 1: The fellowship of TET. *J. Pathol.* **213**, 4–20 (2007).

37. K. Müller, R. Engesser, J. Timmer, M. D. Zurbriggen, W. Weber, Orthogonal optogenetic triple-gene control in mammalian cells. *ACS Synth. Biol.* **3**, 796–801 (2014).

38. K. Müller, R. Engesser, S. Metzger, S. Schulz, M. M. Kämpf, M. Busacker, T. Steinberg, P. Tomakidi, M. Ehrbar, F. Nagy, J. Timmer, M. D. Zubriggen, W. Weber, A red/far-red light-responsive bi-stable toggle switch to control gene expression in mammalian cells. *Nucleic Acids Res.* **41**, e77 (2013).

39. F. Liu, Y. K. Song, D. Liu, Hydrodynamics-based transfection in animals by systemic administration of plasmid DNA. *Gene Ther.* **6**, 1258–1266 (1999).

40. B. S. Schuster, E. H. Reed, R. Parthasarathy, C. N. Jahnke, R. M. Caldwell, J. G. Bermudez, H. Ramage, M. C. Good, D. A. Hammer, Controllable protein phase separation and modular recruitment to form responsive membraneless organelles. *Nat. Commun.* **9**, 2985 (2018).

41. E. M. Zhao, N. Suek, M. Z. Wilson, E. Dine, N. L. Pannucci, Z. Gitai, J. L. Avalos, J. E. Toettcher, Light-based control of metabolic flux through assembly of synthetic organelles. *Nat. Chem. Biol.* **15**, 589–597 (2019).

42. C. D. Reinkemeier, G. E. Girona, E. A. Lemke, Designer membraneless organelles enable codon reassignment of selected mRNAs in eukaryotes. *Science* **363,** eaaw2644 (2019).

43. J. Wang, J.-M. Choi, A. S. Holehouse, H. O. Lee, X. Zhang, M. Jahnel, S. Maharana, R. Lemaitre, A. Pozniakovsky, D. Drechsel, I. Poser, R. V. Pappu, S. Alberti, A. A. Hyman, A molecular grammar governing the driving forces for phase separation of prion-like RNA binding proteins. *Cell* **174**, 688–699.e16 (2018).

44. D. G. Gibson, L. Young, R. Y. Chuang, J. C. Venter, C. A. Hutchison III, H. O. Smith, Enzymatic assembly of DNA molecules up to several hundred kilobases. *Nat. Methods* **6**, 343–345 (2009).

45. H. M. Beyer, P. Gonschorek, S. L. Samodelov, M. Meier, W. Weber, M. D. Zurbriggen, AQUA cloning: A versatile and simple enzyme-free cloning approach. *PLOS ONE* **10**, e0137652 (2015).

46. K. Müller, R. Engesser, S. Schulz, T. Steinberg, P. Tomakidi, C. C. Weber, R. Ulm, J. Timmer, M. D. Zurbriggen, W. Weber, Multi-chromatic control of mammalian gene expression and signaling. *Nucleic Acids Res.* **41**, e124 (2013).

47. J. Schindelin, I. Arganda-Carreras, E. Frise, V. Kaynig, M. Longair, T. Pietzsch, S. Preibisch, C. Rueden, S. Saalfeld, B. Schmid, J.-Y. Tinevez, D. J. White, V. Hartenstein, K. Eliceiri, P. Tomancak, A. Cardona, Fiji: An open-source platform for biological-image analysis. *Nat. Methods* **9**, 676–682 (2012).

48. A. Raue, B. Steiert, M. Schelker, C. Kreutz, T. Maiwald, H. Hass, J. Vanlier, C. Tönsing, L. Adlung, R. Engesser, W. Mader, T. Heinemann, J. Hasenauer, M. Schilling, T. Höfer, E. Klipp, F. Theis, U.

Klingmüller, B. Schöberl, J. Timmer, Data2Dynamics: A modeling environment tailored to parameter estimation in dynamical system. *Bioinformatics* **31**, 3558–3560 (2015).

49. A. C. Hindmarsh, P. N. Brown, K. E. Grant, S. L. Lee, R. Serban, D. E. Shumaker, C. S. Woodward, SUNDIALS: Suite of nonlinear and differential/algebraic equation solvers. *ACM Trans. Math. Softw.* **31**, 363–396 (2005).

50. T. F. Coleman, Y. Li, An interior trust region approach for nonlinear minimization subject to bounds. *SIAM J. Optim.* **6**, 418–445 (1996).

51. C. L. Tucker, Manipulating cellular processes using optical control of protein–protein interactions. *Prog. Brain Res.* **196**, 95–117 (2012).

52. C. Kreutz, A. Raue, J. Timmer, Likelihood based observability analysis and confidence intervals for predictions of dynamic models. *BMC Syst. Biol.* **6,** 120 (2012).

53. A. Raue, C. Kreutz, T. Maiwald, J. Bachmann, M. Schilling, U. Klingmüller, J. Timmer, Structural and practical identifiability analysis of partially observed dynamical models by exploiting the profile likelihood. *Bioinformatics* **25**, 1923–1929 (2009).

54. H. M. Beyer, R. Engesser, M. Hörner, J. Koschmieder, P. Beyer, J. Timmer, M. D. Zurbriggen, W. Weber, Synthetic biology makes polymer materials count. *Adv. Mater.* **30**, e1800472 (2018).

55. D. Hinkley, Predictive likelihood. *Ann. Statist.* **7**, 718–728 (1979).